Available online at www.sciencedirect.com

ScienceDirect

Underground Space 25 (2025) 99–131

www.keaipublishing.com/undsp

Research Paper

Seismic resilience analysis of high-speed railway tunnels across fault zones using ensemble learning approach

Lianjie Yang [b], Chunlei Xin [a,b], Zhao Wang [c,*], Xinyuan Yu [d], Iman Hajirasouliha [d], Wenkai Feng [a,b]

[a] State Key Laboratory of Geohazard Prevention and Geoenvironment Protection, Chengdu University of Technology, Chengdu 610054, China
[b] College of Environment and Civil Engineering, Chengdu University of Technology, Chengdu 610054, China
[c] Institute for Transport Studies, University of Leeds, Leeds LS2 9JT, UK
[d] School of Mechanical, Aerospace and Civil Engineering, The University of Sheffield, Sheffield S1 3JD, UK

Received 25 January 2025; received in revised form 29 March 2025; accepted 11 April 2025
Available online 20 September 2025

Abstract

Severe damage to the Daliang high-speed railway tunnel during earthquakes primarily results from the dynamic interplay between fault dislocation and intense seismic forces near fault lines, accompanied by their complex feedback mechanisms. This study introduces a novel hybrid finite element model to explore the impact of fault dislocation-induced earthquakes on tunnel lining integrity. The influence of seismic characteristics on factors such as peak ground acceleration, tunnel structure form, and the shear modulus of surrounding rock is analyzed. Extensive numerical simulations investigate the coupling effects of faults and various seismic motions on tunnel structures. Additionally, a rapid resilience assessment model for tunnels crossing strike-slip faults is developed using the Adaboost algorithm. This model evaluates the seismic fragility and resilience of such tunnels, offering insights into the anti-seismic behaviors of three distinct tunnel lining configurations under the combined stresses of fault dislocation and significant seismic activity. Furthermore, the fault damage characteristics of the crossing-fault high-speed railway tunnel are assessed, based on real earthquake damage classification and current seismic codes. Findings demonstrate that the evaluation model is both highly accurate and efficient, serving as an effective alternative to traditional nonlinear time-history analysis of tunnel structures. Research shows that critical factors influencing seismic fragility and resilience include the structural design of the tunnel, shear modulus of the surrounding rock, peak ground acceleration, and tunnel height. Simulations reveal that tensile and compressive damage are significantly reduced in circular tunnels with a shock-absorbing joint compared to original tunnel prototypes. Overall, damage assessments from actual faults in crossing-fault high-speed railway tunnels correlate well with numerical predictions, providing essential references for structural recovery and safety evaluations post-earthquake.

Keywords: Tunnel engineering; Lining structure; Strike-slip seismic fault; Ensemble learning; Seismic resilience

1 Introduction

Fault-crossing tunnels are particularly susceptible to severe seismic damage due to fault dislocation and strong seismic motion, especially during high-magnitude earthquakes. For instance, the 2008 Wenchuan earthquake, triggered by the Longmenshan fault zone, caused severe damage to the Longdongzi and Longxi Tunnels (Qu et al., 2021). Similarly, the 2022 Menyuan earthquake, associated with the Lenglongling fault zone (LLLF), resulted in substantial dislocation damage to the Daliang Tunnel (Liu et al., 2022; P. Chen et al., 2023). More recently, the 2023 earthquake in Turkey damaged railway infrastructure near Ozan village (Aydan et al., 2024). Historical data indicate that damage to tunnels crossing fault lines is typically severe, making their repair or reconstruction exceptionally challenging.

* Corresponding author.
E-mail address: z.wang13@leeds.ac.uk (Z. Wang).
Peer review under the responsibility of Tongji University

https://doi.org/10.1016/j.undsp.2025.04.011

Enhancing the seismic resilience of tunnels in active fault zones has therefore become a critical challenge for engineering projects. Tunnel resilience refers to the fragility and risk of tunnel structures under seismic loading as well as their capacity to withstand disaster impacts and recover swiftly. Although underground structures generally demonstrate better seismic performance than above-ground structures, past earthquake events have shown that high-speed railway tunnels crossing fault zones remain vulnerable to considerable damage (Chen et al., 2020; Cui et al., 2022a). The ongoing implementation of national strategies, such as "A Country with Strong Transportation Network" and "China's Western Development Strategy", is driving the construction of major tunnel projects in areas with active seismic faults. Consequently, ensuring the seismic safety of these tunnel structures has become imperative, with tunnel resilience emerging as a vital metric for assessing seismic safety.

Earlier studies primarily relied on expert judgment and historical data; however, numerical simulation technology has now become a critical analysis method (Jiang et al., 2024). Cui et al. (2022b) developed a large-scale underground engineering model using FLAC3D and established a peak ground acceleration (PGA) index-based earthquake damage prediction method. Jiang et al. (2022) confirmed through soil-structure finite element analysis that site conditions significantly influence the probability of earthquake damage by altering structural stiffness and burial depth. Moayedifar et al. (2019) derived the PGA fragility curve for mountain tunnels based on a 2D finite element model. Regarding resilience assessment, Fabozzi et al. (2018) developed a risk early warning framework for high-speed railway tunnel systems to quantify economic losses under varying levels of intensification. Han et al. (2023) proposed an innovative three-dimensional (3D) spatial model to reveal the dynamic evolution of tunnel composite performance and repair costs during the disaster process. H. Huang et al. (2016, 2017) developed a recoverable model for shield tunnel overload and the vulnerable surface theory for double-intensity earthquakes, enabling systematic analysis from disaster damage assessment to recovery performance. Xin et al. (2019) proposed a buffer layer parameter optimization method to enhance structural damping performance through the adjustment of material and geometric parameters. The existing studies still have theoretical gaps regarding the seismic mechanism of crossing-fault tunnel linings and the rapid resilience assessment of high-speed railway tunnels under the seismic trigger effect of active faults. There is an urgent need to develop an intelligent evaluation system based on multi-physical field coupling.

Incremental dynamic analysis (IDA), a primary method for seismic fragility assessment, relies on nonlinear time-history analysis, leading to low computational efficiency and challenges in addressing uncertainties in geometric parameters, material properties, and structural configurations of tunnels crossing fault zones and mountain tunnels. Repeatedly generating deterministic fragility curves significantly increases computational burden, particularly when assessing key parameter influences, thereby limiting the engineering applicability of quantitative tunnel seismic resilience evaluation under complex geological conditions. In recent years, several innovative methods have emerged in nonlinear finite element analysis. Rabczuk et al. (2004, 2010) developed a meshless EEGP method for efficiently simulating complex dynamic cracks using local particle enrichment and an implicit crack activation mechanism. Firouzi et al. (2023) developed a time-varying deformation prediction model for viscoelastic film materials, utilizing deformation gradient tensor decomposition and implicit trapezoidal time integration to enhance the accuracy of large deformation analysis. Karami et al. (2021) integrated gene expression programming (GEP) and multiple linear regression (MLR) to develop a predictive model for the fire-bearing capacity of composite honeycomb steel beams, overcoming the limitations of traditional testing methods. Samaniego et al. (2020) embedded deep neural networks (DNNs) into the energy variational framework to directly solve mechanical partial differential equations, addressing challenges in multi-field coupling and high-order continuity. Shishegaran et al. (2021a, 2023) achieved intelligent prediction of water pressure-induced damage evolution in fiber-reinforced concrete tunnels by integrating GEP with nonlinear finite element modeling. Collectively, these studies demonstrate that integrating machine learning with advanced numerical methods significantly improves computational efficiency and simulation reliability in complex tunnel engineering.

Several scholars have investigated the application of advanced machine learning techniques in structural engineering. Regarding materials, Shishegaran et al. (2020a) investigated the PVP-modified polyether sulfone membrane in combination with GEP to optimize ultrafiltration process parameters, achieving efficient removal of the anionic surfactant SDS from wastewater. In structural engineering prediction and evaluation, Zhang et al. (2025) developed a CNN-based 3D numerical model framework to quantify the dynamic response and resilience of tunnels subjected to explosion loads. Lyu et al. (2024) introduced an LSTM-CFD fusion approach to enable intelligent tracking of flammable gas leakage through time series data analysis. Huang et al. (2023) developed a 1D-CNN-PDEM non-parametric model to enhance the accuracy of time-dependent seismic vulnerability assessment of subway stations. Shishegaran et al. (2020b, 2021b) and Naghsh et al. (2021) integrated machine learning algorithms with multi-disciplinary methods to enhance model performance in complex scenarios. They further combined nonlinear finite element analysis with GEP, the adaptive neuro-fuzzy inference system (ANFIS), and other algorithms. A multi-scenario predictive system for structural engineering was developed. Regarding tunnel fragility analysis and risk assessment, Sun et al. (2018) pioneered a support vector machine multi-classification model to predict tunnel extru-

sion deformation effectively. Z. Huang et al. (2022a) integrated finite element methods and SVM algorithms to develop an intelligent system for generating vulnerability curves of mountain tunnels and concrete dams. Regarding the modeling of nonlinear geological problems, Adoko et al. (2013) used MARS and ANN to develop a convergence deformation prediction model for high-speed railway soft rock tunnels, offering a new paradigm for analyzing complex geological conditions. Hasanpour et al. (2020) developed a dynamic assessment framework for TBM extrusion risk based on ANN and Bayesian networks through multi-source data fusion, enabling the coupling analysis of geological and construction parameters. L. Wang et al. (2023) innovatively combined probabilistic seismic design methods with uncertainty quantification to create a collaborative assessment system for the seismic vulnerability and resilience of mountain tunnels. Despite these advancements, research on the seismic resilience analysis and reinforcement strategies for tunnel linings under the combined impacts of fault dislocation and intense seismic activity, facilitated by machine learning, remains in the preliminary stages.

Advances in seismic resilience enhancement for fault-zone tunnels primarily focus on two aspects: optimizing material modifications and developing novel seismic structures. Dai et al. (2023) investigated the vibration isolation mechanism of glass fiber-reinforced concrete lining through shaking table tests and systematically analyzed the effects of fiber content and isolation layer thickness on the dynamic response intensity in key areas. Long et al. (2023) developed a shape memory alloy flexible ring joint, whose unique deformation adaptability enhanced the tunnel's longitudinal stiffness adjustment and energy dissipation efficiency. Wang et al. (2024) identified typical weak zones in the 45° conjugate direction of the tunnel lining through model tests in the fault fracture zone. Although the damping layer reduced peak internal forces at the arch foot and spandrel, it did not alter the overall dynamic response of the structure. Xin et al. (2018, 2020, 2022) and Wen et al. (2021) compared the seismic performance of damping joints, buffer layers, and casing structures, finding that flexible joints enhanced deformation coordination through stiffness matching. The buffer layer mitigates bond damage risk in the surrounding rock through interface decoupling. The casing structure offers dual advantages: enhancing resistance during earthquakes and optimizing post-earthquake repair efficiency. These studies highlight key strategies for enhancing tunnel seismic performance through damping measures. By mitigating seismic damage and facilitating post-earthquake recovery, this study provides theoretical support and technical guidance for enhancing the long-term seismic resilience of high-speed railway tunnels crossing strike-slip seismogenic faults.

This study establishes a rapid resilience assessment framework for high-speed railway tunnels crossing strike-slip seismogenic faults. Centered on numerical simulations of the dynamic interaction between surrounding rock and tunnel, this study generates high-quality datasets to support resilience analysis, optimizes model performance using the Adaboost algorithm, and integrates multi-source modeling techniques to enhance prediction accuracy and flexibility. The developed damage prediction model effectively quantifies the relationship between seismic intensity, tunnel structure, surrounding rock properties, and damage index, enabling key parameter selection and input variable reduction. Based on this, the coupling mechanism of fault dislocation and seismic motion on tunnel fragility and resilience is thoroughly analyzed, followed by a comprehensive evaluation of seismic performance and an investigation into the regulatory effects of various repair strategies on tunnel seismic response. Finally, using the Daliang Tunnel project as a case study, the model's accuracy in identifying damage features and assessing recovery capability in real earthquake events is validated, providing a theoretical foundation and technical support for risk mitigation and resilience enhancement in tunnel engineering across strike-slip seismogenic fault.

2 Seismic resilience framework for tunnels

This study proposes a resilience evaluation framework for high-speed railways affected by across strike-slip seismic events (as shown in Fig. 1(a)). The Adaboost algorithm identified key variables, including tunnel parameters, surrounding rock properties, and seismic motion intensity. PGA was the main input, and the lining damage index was the output. By integrating fault dislocation and seismic excitation, a nonlinear seismic response dataset was constructed. The trained model replaces numerical simulations and shaking table tests to generate tunnel seismic fragility curves. A quantitative resilience evaluation system integrates multi-source disaster data for analyzing earthquake damage evolution and structural resilience.

In the tunnel seismic resilience framework, an initial seismic damage analysis is performed. Based on existing research and field investigations, this analysis determines earthquake damage extent. Seismic fragility analysis assesses structural performance degradation under specific conditions. The structural recovery time is estimated to develop an appropriate recovery model. This forms a resilience analysis model, evaluated with quantitative indicators. The process is shown in Fig. 1(b).

2.1 Tunnel seismic hazard analysis

Based on the existing active fault zone distribution map and the study of strong earthquake areas, the seismic damage characteristics of relevant sites are described using the seismic motion intensity parameters (IM). This method can calculate the probability of exceeding a specific seismic demand level during a defined operational period or determine the spatial distribution of IM during site-specific seismic response analyses of high-speed railway tunnels (Huang et al., 2020). Due to the uncertainty of seismic

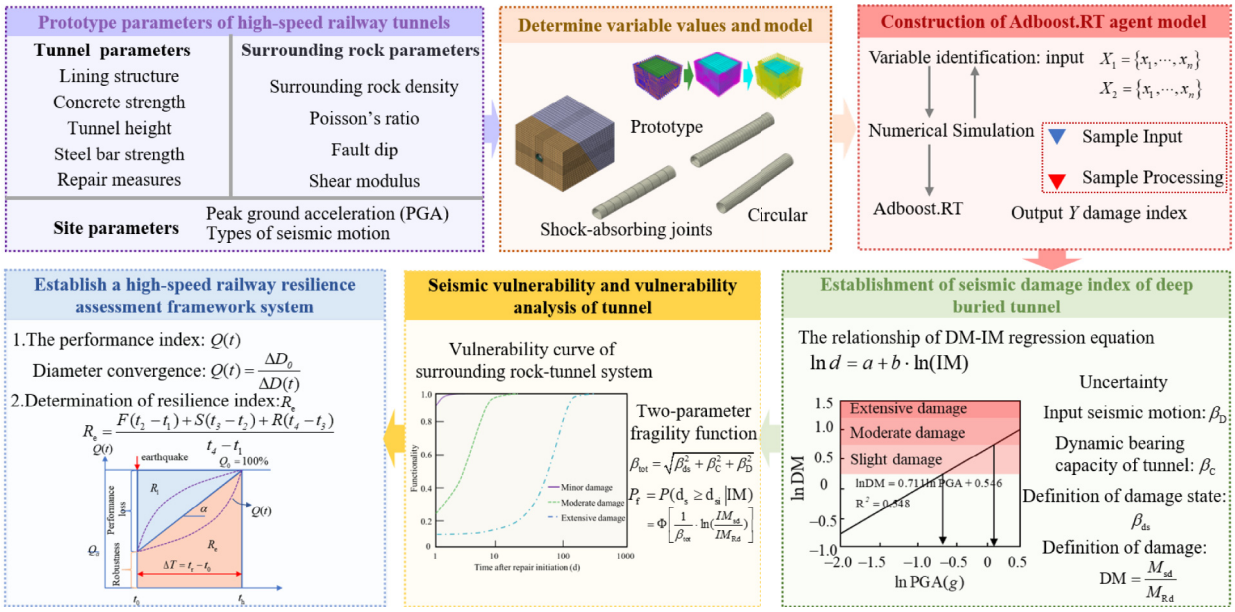

(a)

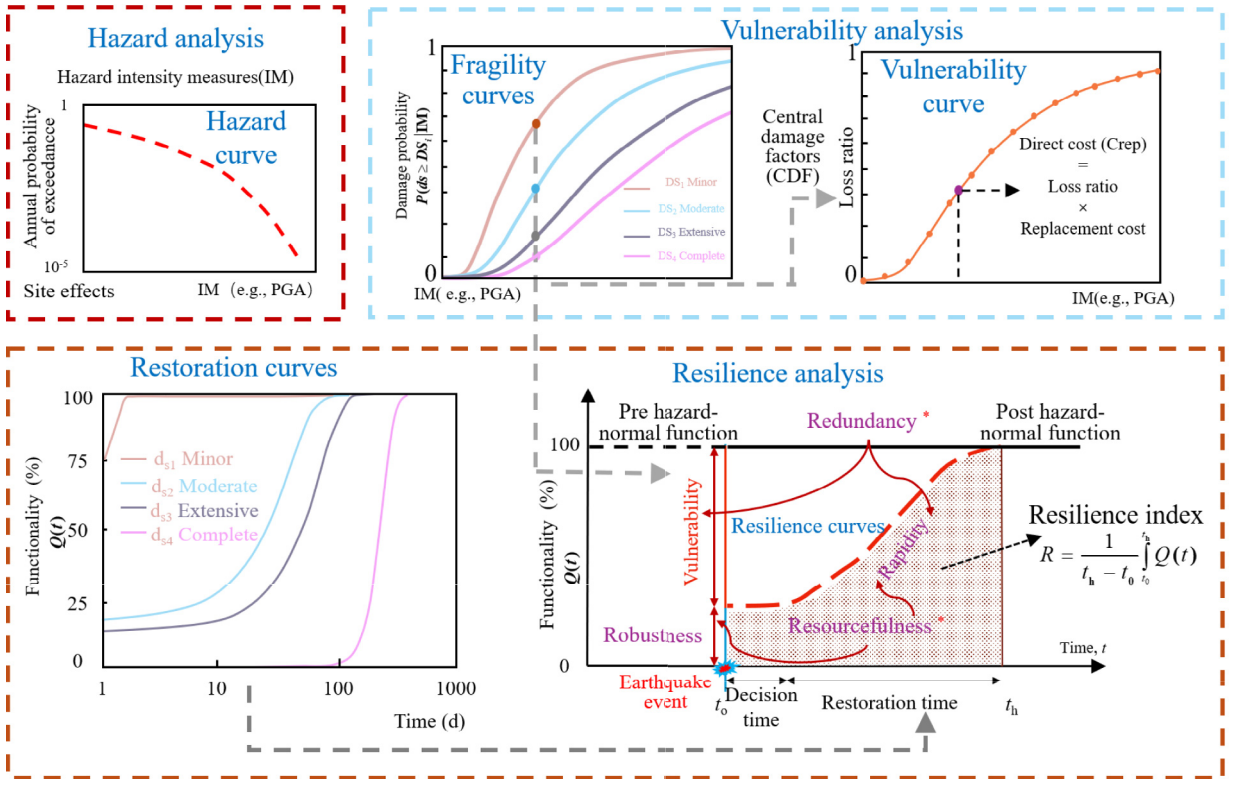

(b)

Fig. 1. Seismic resilience framework for tunnels. (a) Resilience evaluation framework of high-speed railway across strike-slip seismogenic fault, and (b) seismic resilience evaluation framework of tunnel.

motion, quantification is a critical factor. Common dynamic loads for underground structures include PGA, peak ground velocity (PGV), and permanent ground displacement (PGD). For high-speed railway tunnels, PGA and PGV are generally better correlated with structural damage and can be used to characterize earthquake hazard levels (Zhou et al., 2021). The seismic hazard analysis is designed to identify representative disaster scenarios, including earthquakes, debris flows, and high ground stress, in the tunnel area to evaluate expected losses and the resilience of infrastructure. Additionally, fault dislocation, as the primary hazard, triggers seismic motion, which

in turn leads to additional hazards such as ground shaking, surface rupture, and potentially landslides (illustrated in Fig. 2(b) and (c)). These secondary hazards depend on the primary hazard and form a cascading chain of effects. The multiple hazards identified in the foundational setup are categorized as correlated or cascading hazards (Argyroudis et al., 2020). Figure 2 illustrates the tunnel lining hazard analysis curve in relation to increasing peak ground acceleration.

2.2 Seismic fragility analysis of tunnel structure

The seismic intensity measure directly influences the variability and validity of seismic fragility analysis results, and is a key factor in assessing the seismic fragility of tunnel structures. Thus, selecting an appropriate seismic intensity measure (IM) is a crucial aspect of the seismic fragility analysis of tunnels (Tsinidis et al., 2022). The seismic fragility of the tunnel can be evaluated using a fragility curve, which indicates the probability of the tunnel structure exceeding various damage states under different seismic intensities. This study examines the dynamic interaction between the rock mass and tunnel structure, along with the corresponding demand measures (DM) under various peak acceleration conditions through numerical simulation. Subsequently, based on the calculated DM and corresponding IM, a probabilistic seismic demand model (PSDM) is developed. Following this, the nonlinear time-history results are post-processed to explore the statistical correlation between seismic intensity measures and structural response across each damage state. Cornell et al. (2002) represented the structural seismic demand measure as a log-linear function of the seismic intensity measure (Eq. (1)):

$$\ln d = a + b \cdot \ln(\mathrm{IM}), \tag{1}$$

where d represents the structural seismic demand parameter, IM denotes the seismic motion intensity parameter, a and b signify the regression parameter. In seismic fragility analysis of structures, regression analysis is commonly employed to establish the relationship between seismic DM and seismic IM.

Ultimately, fragility functions are derived from the proposed probabilistic seismic demand model (PSDM) (Huang et al., 2021). In current seismic fragility analyses of tunnels, most fragility curves are characterized by a two-parameter logarithmic distribution model, as illustrated in Eq. (2):

$$P_{\mathrm{f}}(d_{\mathrm{s}} \geq d_{si}|\mathrm{IM}) = \Phi\left[\frac{1}{\beta_{\mathrm{tot}}} \cdot \ln\left(\frac{\mathrm{IM}}{\mathrm{IM}_{\mathrm{m}i}}\right)\right], \tag{2}$$

where $P_{\mathrm{f}}(\cdot)$ represents the probability of exceeding a certain failure state d_{s}; Φ denotes the cumulative probability function of the standard normal distribution; $\mathrm{IM}_{\mathrm{m}i}$ represents the threshold of the seismic parameter S that causes the i-th failure state; β_{tot} represents the total logarithmic standard deviation, which is a combination of three independent uncertainties and can be expressed by Eq. (3):

$$\beta_{\mathrm{tot}} = \sqrt{\beta_{\mathrm{ds}}^2 + \beta_{\mathrm{C}}^2 + \beta_{\mathrm{D}}^2}, \tag{3}$$

where β_{ds} represents the uncertainty of the failure state, β_{C} accounts for the uncertainty in the tunnel's response and bearing capacity, and β_{D} captures the uncertainty of the input seismic motion. The values of β_{ds} and β_{C} are typically set as 0.4 and 0.3, respectively. The value of β_{D} is determined based on the standard deviation of the damage index calculated from different seismic wave inputs and the deviation of the fitted regression curve (Z. Huang, 2022b).

2.3 Seismic resilience analysis of tunnel structure

2.3.1 Tunnel performance recovery curve

Assessing the seismic resilience of engineering structures is crucial for disaster mitigation; however, existing theoretical frameworks remain underdeveloped. This study examines the variability in post-earthquake recovery curves of tunnels with identical damage states, utilizing the FEMA (2020) empirical model to characterize time-dependent restoration processes (as shown in Fig. 3). The proposed methodology quantifies recovery velocity, completeness, and total duration, addressing the limitations of conventional linear recovery assumptions. Key functionalities include bottleneck identification, resource allocation

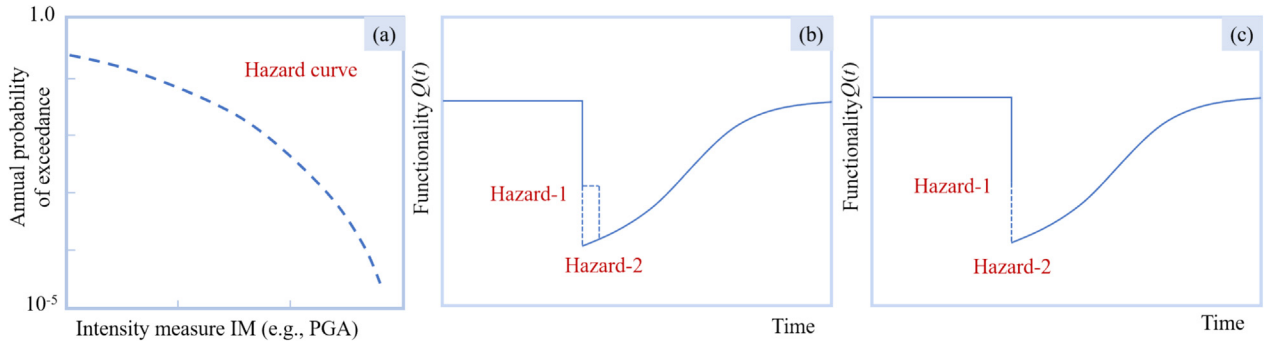

Fig. 2. Seismic damage analysis curve.

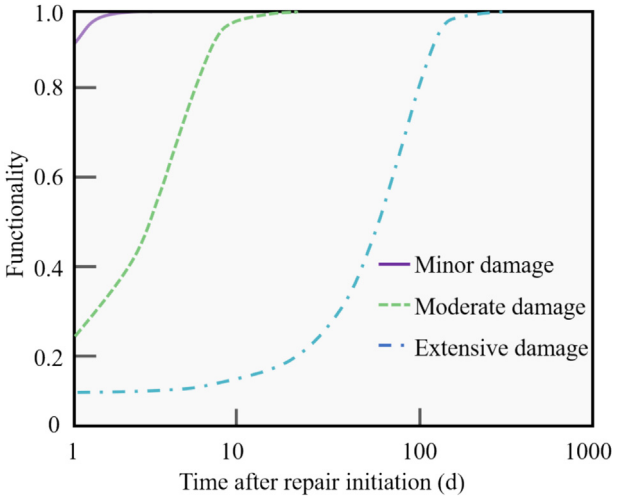

Fig. 3. Estimation of the functionality function $Q(t)$ of a tunnel.

optimization, and stage-specific intervention planning, forming a dynamic decision-making framework for prioritizing post-disaster rehabilitation efforts. This approach enhances resilience evaluation by incorporating nonlinear recovery dynamics into infrastructure performance assessments.

2.3.2 Definition and metric of tunnel resilience

Throughout the extended service life of high-speed railway tunnels, the durability of concrete lining structures progressively diminishes. Additionally, infrequent low-probability risks and adverse environmental conditions (such as earthquakes, debris flows, and high ground stresses) may further compromise the integrity of the lining structure. Various modes of seismic damage correlate with different degrees of structural performance loss in the tunnel lining. However, quantitative analyses of structural performance loss remain inadequate. To address this issue, a resilience framework can assess the extent of degradation in a tunnel's structural performance following an adverse environmental disturbance, as well as its ability to recover rapidly from damage, thereby estimating a reasonable repair time, as shown in Fig. 4 (X. S. Chen et al., 2023).

Initially, consider the performance decline caused by the time effect under normal conditions, referred to as normal performance. The period from the occurrence of a disaster t_1, such as a strong earthquake, to the restoration of the tunnel to operational status (t_4) includes a duration of structural performance changes (Δt). Figure 4 illustrates this transition with a dashed arrow line. When the tunnel experiences strong earthquake and fault coupling at t_1, its structural performance will sharply decline to the level at t_2. The interval from t_2 to t_3 represents the decision-making period for emergency rescue and repair measures. It is assumed that if repair actions are initiated at t_3, the tunnel will return to an operational performance level by t_4. Eventually, the tunnel may achieve a stable state. Table 1 provides a detailed explanation of the various dimensions of resilience depicted in this figure. Similar to other infrastructure, tunnel resilience must possess the capacity to withstand performance disturbances, exhibiting high robustness or low fragility, as well as the ability to rapidly recover to an acceptable performance level (Tsinidis et al., 2024a).

By quantifying structural damage and recovery potential to assess system resilience, the elasticity index integrates structural strength, functional durability, and repair cycle parameters in tunnel engineering, enabling predictive analysis and optimized decision-making for post-disaster recovery. Considering the nonlinear characteristics of structural properties and the limitations of traditional conditional probability methods, this study establishes a multi-dimensional seismic resilience evaluation system for tunnel linings based on the resilience model developed by Huang et al. (2016).

$$R_e = \frac{F(t_2 - t_1) + S(t_3 - t_2) + R(t_4 - t_3)}{t_4 - t_1}. \tag{4}$$

In the formula, the three weight coefficients represent area ratios derived from the transition curves, failure curves $F(t)$, evolution curves $S(t)$, and recovery curves $R(t)$ depicted in Fig. 4. Variations in tunnel environmental conditions and the types of repair measures implemented after an earthquake can lead to different scenarios. Figure 5 illustrates several general types of performance change curves. Notably, during the damage stage, structural properties may degrade in ductile F_1, linear F_2, or brittle F_3 modes. Otherwise, the duration of the repair decision process significantly impacts damage recovery, repair costs, and overall recovery efficiency of tunnel linings. An earlier decision can reduce costs and requirements, helping to maintain the tunnel's designed service life. Therefore, the post-earthquake decision-making stage S_1 is assumed to lead to a further damage stage. Following tunnel repair, structural performance may manifest in one of three scenarios: case 1 better than the initial performance $Q_0(R_1)$, case 2 equal to the initial performance $Q_0(R_2, R_3)$, or case 3 lower than the initial performance $Q_0(R_4)$. This study focuses on the degree and mode of degradation of post-earthquake structural performance, assuming that the tunnel structure returns to its initial performance after repair, corresponding to case 2.

2.3.3 Performance indicators of tunnel linings

The above definition and measurement of the resilience model can also be applied to the conditions and performance indices of tunnel lining under the coupled action of fault and seismic motion. Under the coupling of fault dislocation and seismic motion, the resilience of high-speed railway tunnels decreases sharply, with damage states ranging from slight to complete. The selection of the tunnel lining performance index is essential for determining the resilience indices, as it reflects the tunnel's post-earthquake damage. Therefore, the performance index must be established before deriving the performance

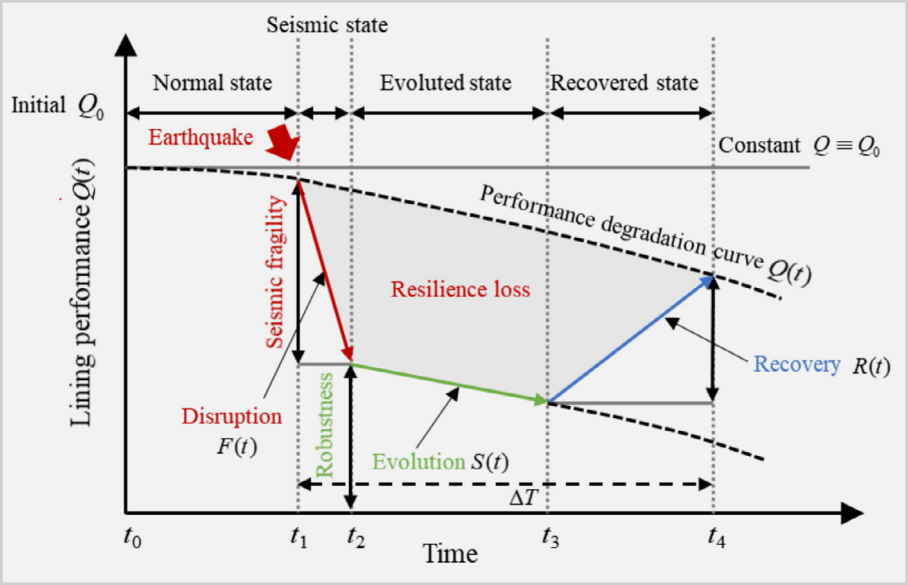

Fig. 4. Performance variation trend in tunnel resilience analysis.

Table 1
System properties in the frame of resilience.

Dimension	Symbol	System property
Degradation	$Q(t)$	Performance degradation due to time effect
Robustness	$R_0 = f(t_f)$	Residual of performance after disruption
Fragility	$V_n = Q(t_f) - f(t_f)$	Loss of performance after disruption
Rapidity	$\Delta T = t_4 - t_1$	Whole time duration for disrupted state of system

degradation curve to reflect changes in tunnel lining performance. According to D. Huang et al. (2022), the primary defects of tunnel systems post-disaster and the prioritization of common defect risks under FEMA are illustrated in Fig. 6. Consequently, in this study, the selected tunnel lining diameter convergence is used as an index for evaluating lining performance (Lin et al., 2022), defined as follows:

$$Q(t) = \frac{\Delta D_0}{\Delta D(t)}, \tag{5}$$

where ΔD_0 is the initial convergence when the tunnel is built, and $\Delta D(t)$ is the convergence at time t.

To assess the influence of various environmental factors and the effectiveness of rapid recovery or adaptation strategies for tunnel structures after an earthquake, it is essential to evaluate the resilience of the tunnel lining structure, following the calculation of resilience and structural performance. This study assesses the resilience evaluation indices proposed by Z. Huang et al. (2022c), as presented in Table 2.

The resilience model employed in this study characterizes tunnel damage resulting from the coupled effects of fault activity and seismic motion, including cracks in the tunnel lining, extensive lining shedding, and tunnel dislocation. Notably, this study does not account for delays due to aftershock activity, site repairs, and evaluations.

3 Methodology

3.1 Ensemble learning

Advances in machine learning have greatly improved tunnel disaster resilience analysis. This study applies an integrated learning algorithm (Decò et al., 2013) to address the limitations of traditional methods in handling engineering uncertainties. Multiple base learners are integrated using voting or weighting to enhance prediction accuracy. This approach mitigates overfitting in multi-dimensional tunnel performance analysis, improves generalization, and addresses limitations of the linear damage hypothesis. The proposed framework, leveraging data-driven feature extraction, captures the nonlinear relationship between structural degradation and recovery potential, advancing intelligent resilience assessment.

Among various ensemble learning algorithms, Adaboost is one of the most widely used enhancement algorithms, featuring adaptive resampling technology for selecting training samples. In each iteration, the selection frequency of misclassified data from the previous classifier is higher

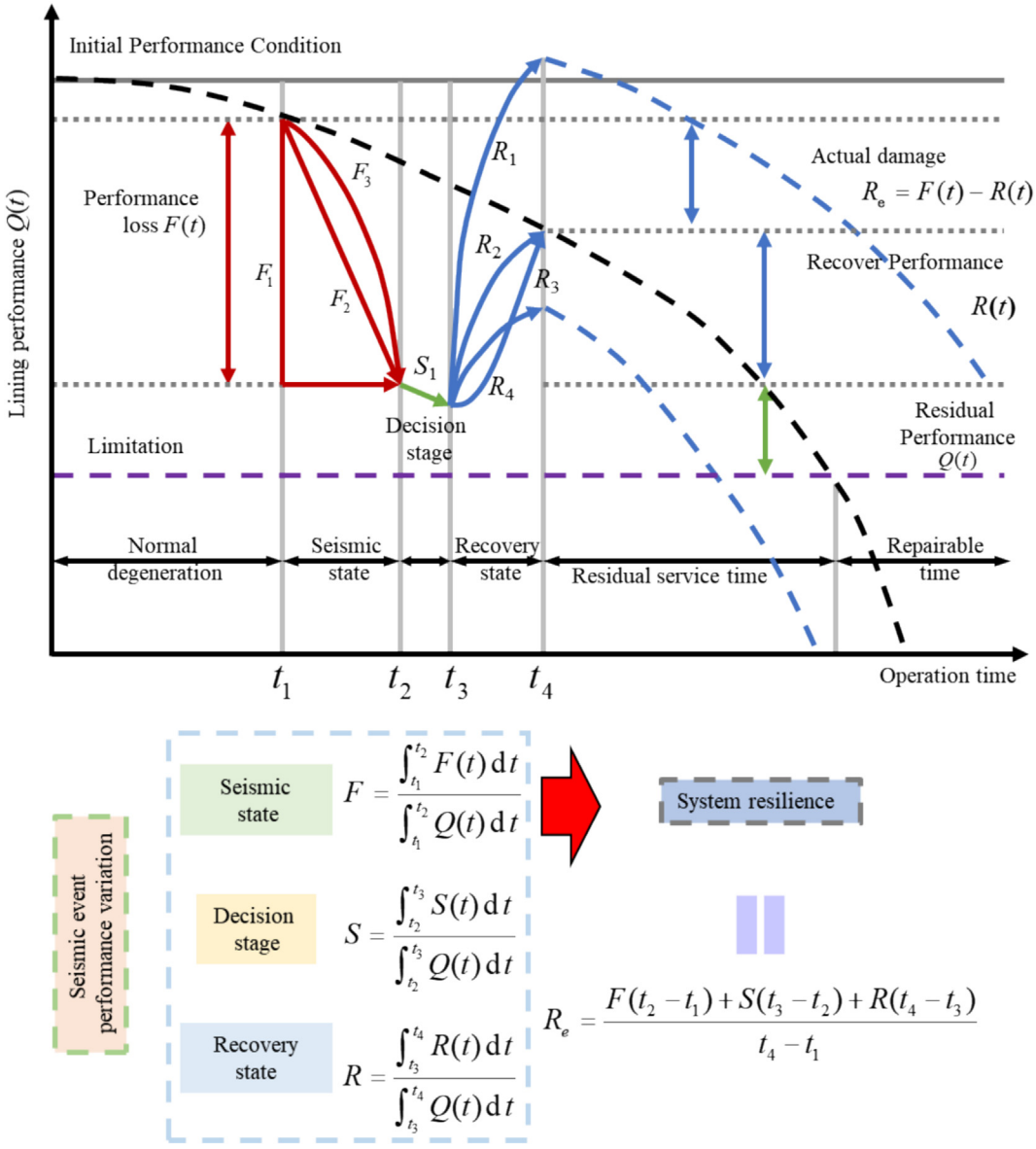

Fig. 5. Trend of tunnel performance and cumulative damage under the effect of fault dislocation triggering strong earthquakes.

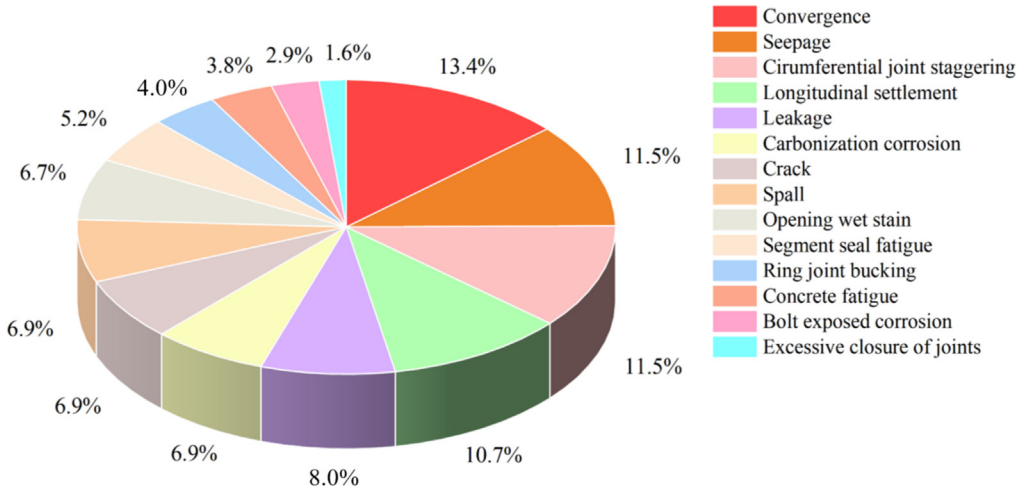

Fig. 6. Risk priority of common defects under FEMA.

Table 2
Classification of resilience grades.

Standard	Resilience		Resilience grade
	Robustness	Rapidity	
High	Better	Excellent	$0.9 \le R < 1.0$
Moderate	Good	Fast	$0.6 \le R < 0.9$
Low	General	Moderate	$0 \le R < 0.6$
No	Poor	Slow	$R < 0$

than that of correctly classified data, allowing the new classifier to focus on the reweighted misclassified samples. Each iteration adjusts the weights of the data set, allowing the subsequent integration models to focus more on the previously misclassified data (Hong et al., 2018; Xing et al., 2024).

3.2 Principle of the Adaboost algorithm

In geotechnical engineering, commonly used ensemble learning algorithms include Adaboost and its extensions: Adaboost.M1, M2, R, R2, and RT. For a robust ensemble model, base predictors should be reasonable, effective, and independent (Wu et al., 2020). Traditional Adaboost uses a single-type base classifier. Different base models are selected based on sample distributions during training. This study modifies Adaboost.RT by incorporating diverse base learners to construct the final ensemble framework.

The Adaboost.RT algorithm is an improved version based on Adaboost regression algorithms such as Adaboost.R and Adaboost.R2. A threshold is introduced in the Adaboost algorithm, dividing the training set into "satisfactory" and "disappointing" categories by comparing the training error with the threshold. Consequently, the regression problem is transformed into a straightforward binary classification problem (Tian et al., 2010). The specific process of the Adaboost.RT algorithm is illustrated in Fig. 7.

3.3 Establishment of an integrated multi-learning model based on the Adaboost.RT algorithm

To develop an ensemble learning model with robust generalization capabilities, it is ideal for the weak learners within the ensemble to be as independent as possible. However, achieving complete independence is often challenging in practical applications. Therefore, the common practice involves selecting the same base learning model, utilizing different training samples to generate distinct weak learners. In this study, various base learning models are chosen as weak learners to build strong learning models with enhanced generalization capability. Given the limited amount of tunnel engineering data, which falls into the category of small sample data, there is a need for a model adept at processing such datasets effectively. Additionally, considering the factor of training time, this study selects

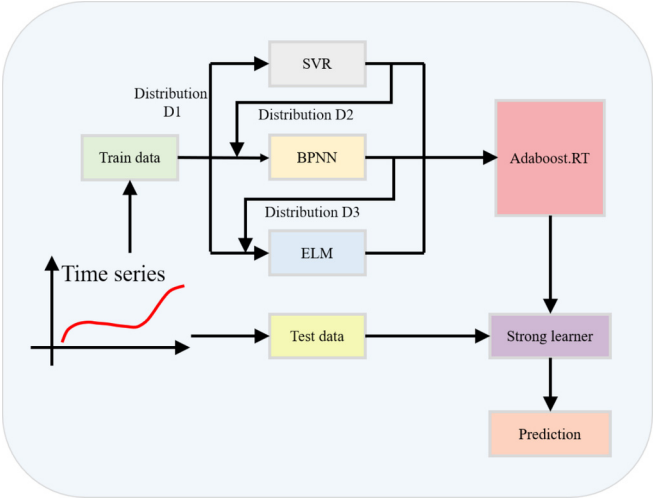

Fig. 7. Work flow of Adaboost.RT algorithm.

three base learning models that are well-suited for small sample data and demonstrate robust learning capabilities: support vector regression (SVR), back propagation (BP), and extreme learning machine (ELM) (Du et al., 2024).

Among the selected base classifiers, SVR, derived from SVM, is noted for its robust generalization capabilities. It effectively addresses challenges associated with small sample sizes, overfitting, high dimensionality, and local minima, making it particularly suitable for complex engineering problems (Gu et al., 2015). The BP network demonstrates significant adaptability, self-organization, self-learning capability, and nonlinear mapping ability, overcoming the limitations of traditional feedback methods, and has gained widespread use in recent years (Tian et al., 2022). Compared with traditional gradient descent algorithms, the ELM learning machine exhibits faster convergence and higher prediction accuracy, facilitating global optimization (Chai et al., 2023). Table 3 illustrates the specific application of the Adaboost.RT algorithm in high-speed railway tunnels.

In the Adaboost.RT algorithm, the selection of the threshold significantly influences the effectiveness of the algorithm. Currently, there is no established automatic threshold selection algorithm that consistently provides clear and reliable results. Therefore, this study employs a manual approach, adjusting and iteratively refining the threshold to optimize performance.

4 Engineering application and comparison

4.1 Study area

On January 8, 2022, at 1:45 AM, an M_s 6.9 earthquake struck Menyuan County, Qinghai Province, China (101.26°E, 37.77°N). The earthquake was associated with the Lenglongling fault (F5) in the middle-west section of the Qilian-Haiyuan fault, which is located on the northeastern margin of the Qinghai-Xizang Plateau, which

Table 3
Specific application of the Adaboost.RT algorithm in high-speed railway tunnels.

Algorithm name: Adaboost.RT for resilience analysis of high-speed railway tunnel lining.
Input: Training set $X = \{(x_1, x_2, x_3, y_1), (x_2, x_3, x_4, y_2), \cdots, (x_n, x_{n+1}, x_{n+2}, y_n)\}$, three basic learning models Q_1, Q_2, Q_3, iteration times $T = 3$, threshold value φ, sample weight D_t.
Initialization: Error rate $\varepsilon_t = 0$, iteration times $t = 1$, initialize sample weights $D_t(i) = \frac{1}{n}, i = 1, 2, 3, \cdots n$.
Training: When $t < T$
Step 1: Call the base learner to provide sample weights: $D_t(i) = \frac{1}{m}$.
Step 2: Establish regression model: $f_t(x) = L_t(X, D_t) \rightarrow y$.
Step 3: Calculate the relative error of each training sample: $E_t = \left\lvert \frac{f_t(x_i) - y_i}{y_i} \right\rvert$.
Step 4: Calculate error rate: $\varepsilon_t = \sum_i D_t(i)$, until $E_t(i) = \left\lvert \frac{f_t(x_i) - y_i}{y_i} \right\rvert > \varphi$.
Step 5: Set weight update parameters: $\beta_t = \varepsilon_t^h, (h = 1, 2, 3)$.
Step 6: Update sample weights: $D_{t+1}(i) = \frac{D_t(i)}{Z_i} \times \begin{cases} \beta_t, & E_t(i) \le \varphi \\ 1, & \text{other} \end{cases}$.
Step 7: Adjust according to the Adaboost.RT algorithm.
Step 8: Set $t = t + 1$.
Step 9: Output the integrated learner: $f(x) = \frac{\sum_{t=1}^{T} \lg\left(\frac{1}{\beta_t}\right) f_t(x)}{\sum_{t=1}^{T} \lg\left(\frac{1}{\beta_t}\right)}$.

exhibits pure left-lateral strike-slip characteristics (Zhu et al., 2023; Zhang et al., 2023a) (see Fig. 8). The epicenter was located approximately 4.5 km from the Daliang Tunnel of the Lan(zhou) Xin(jiang) high-speed railway. The primary surface crack formed by the earthquake extends nearly east–west through the mountain above the tunnel's exit. The fracture length on the north side measures approximately 21.5 km, with a maximum displacement of about 3.1 m. On the south side, the fracture length is approximately 3.8 km, with a maximum displacement of about 0.5 m (Zhang et al., 2023b). Daliang Tunnel is a double-track high-speed railway tunnel featuring a 5 m line spacing, a maximum buried depth of approximately 800 m, and a total length of 6567.82 m (Bao et al., 2022). The Menyuan earthquake resulted in a maximum horizontal displacement of 1.78 m along the tunnel's alignment. The segment of the tunnel lining exhibiting the most severe seismic damage measures approximately 350 m, particularly evident in the affected zone of the F5 fault. This segment constitutes 5.33% of the tunnel's total length, while the overall length affected by severe seismic damage accounts for 15.96% of the total length of the tunnel (Y. Wang et al., 2023).

The section of the Daliang Tunnel from K1971+341 to K1971+691 crosses an active fault, where significant seismic damage has occurred, including severe misalignment of the track, lateral extrusion of the side wall, and collapse of the secondary lining. Notably, the maximum uplift height of the track bed is approximately 0.7 m. The rail has twisted and is suspended in a serpentine shape, the fasteners have collapsed, and the entire side of the track plate is damaged. The cover plates of the ditches on both sides were pushed upward, causing the ditch side walls to tilt and partially crush. Additionally, the arches of the lining in certain sections were continuously crushed and fractured. The side wall of the lining at the boundary of the

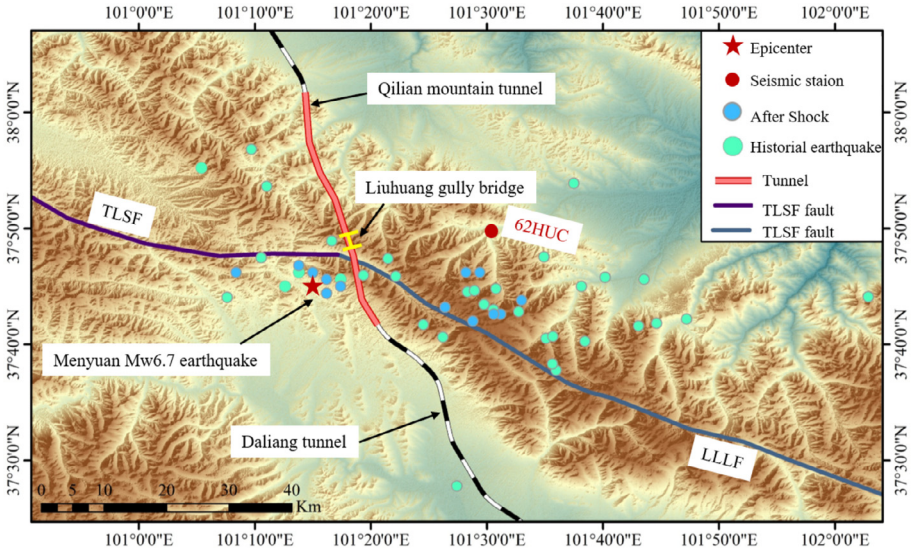

Fig. 8. Earthquake background and location in the Daliang tunnel area.

fault exhibits extrusion failure, with a maximum displacement of approximately 1.8 m on the right wall and about 1.5 m on the left wall. The steel reinforcement is distorted, the waterproof membrane is torn and exposed, and significant left-lateral strike-slip characteristics are evident (as shown in Fig. 9(a) and (b)).

The sections K1970+695 to K1971+341 and K1971 +691 to K1972+093 exhibit severe seismic damage in the

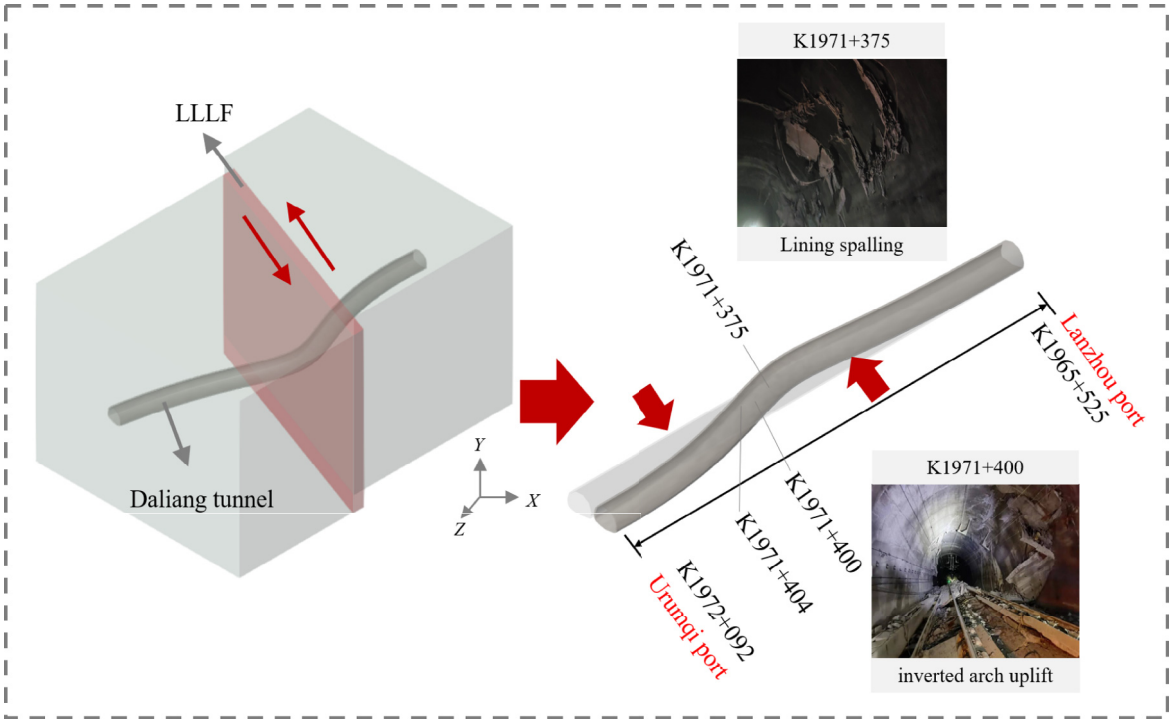

(a)

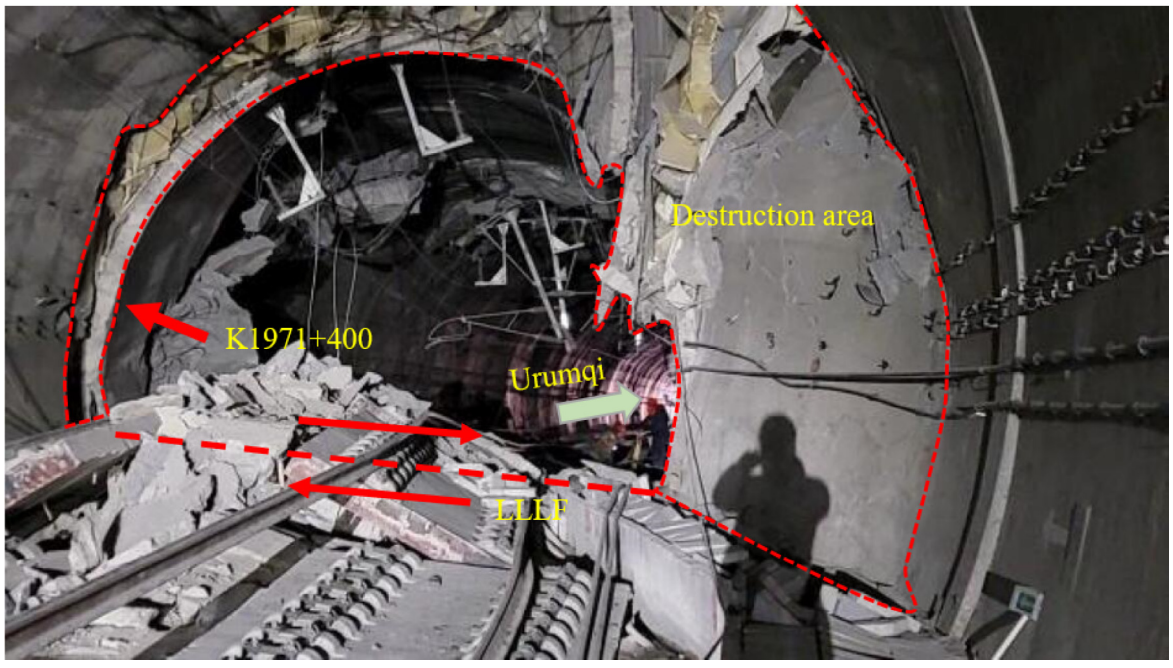

(b)

Fig. 9. Schematic diagram of earthquake damage phenomenon. (a) Overall offset shape and typical extremely serious earthquake damage of Daliang tunnel, and (b) Daliang Tunnel crossing Lenglongling strike-slip active fault and extremely serious earthquake damage morphology.

Daliang tunnel, with the lining misaligned by approximately 10 cm. Additionally, the arch and left wall show significant spalling in 10 locations, covering areas ranging from 0.5 to 15 m^2. The arch and side walls display annular, longitudinal, and oblique discontinuous cracking, with earthquake damage primarily concentrated along the ring. Water seepage is observed in some areas, and longitudinal continuous cracking of the invert filling layer occurs in several sections, alongside cracking in some interior walls of the attached caverns. The severely damaged section is significantly affected by the left-lateral extrusion of the fault; however, the extent of this influence is less severe than that observed in the fault fracture zone. Consequently, crossing-fault tunnel engineering incurs substantial losses and presents challenges for repairing earthquake damage, highlighting the urgent need to enhance seismic resilience.

4.2 Establishment of a 3D finite element model

Using the world's first case of Daliang tunnel damage and repair due to a strong earthquake induced by fault dislocation, an adaptive numerical model is developed. This model, featuring a circular section and a shock-absorbing joint, aligns with field repair technology. It is employed to elucidate the damage mechanisms of various anti-seismic lining measures under coupled effects, providing theoretical and technical support for enhancing the resilience of tunnels across strike-slip seismogenic fault (P. Chen et al., 2024).

A finite element three-dimensional numerical model of the surrounding rock-tunnel interaction was developed, as illustrated in Fig. 10. The fault inclination was set at 60°, and the model consisted of a fixed disk and a moving disk, with the hanging wall designated as the moving disk and the footwall as the fixed disk. The overall dimensions of the model were 120 m × 110 m × 80 m, and the cross-section of the prototype tunnel was horseshoe shaped. Additionally, numerical models were created for both circular sections and shock-absorbing joints to investigate the dynamic response characteristics of the tunnel under different cross-sectional shapes and repair measures. The surrounding rock is classified as Grade V, and the lining

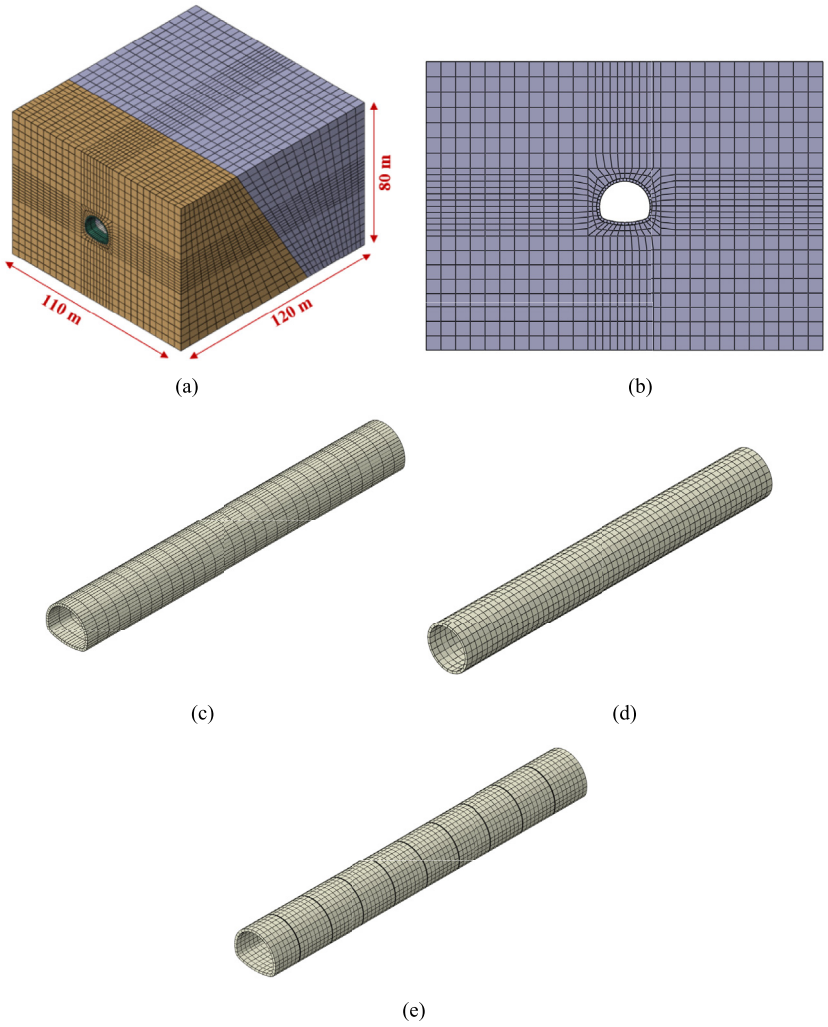

Fig. 10. Three-dimensional finite element numerical calculation model of surrounding rock-tunnel interaction. (a) Overall three-dimensional model, (b) front view of the three-dimensional model, (c) prototype tunnel lining, (d) circular tunnel lining, and (e) shock-absorbing joint tunnel lining.

Table 4
Model material parameters.

Properties	Density (kg/m^3)	Young's modulus, E (GPa)	Poisson's ratio, v	Friction angle (°)	Cohesion (MPa)
Surrounding rock	1800	1.0	0.35	25.3	3.2
Fault	1700	0.9	0.42	20.1	1.5
Lining	2500	31.5	0.2	–	23.4

Table 5
Information of input motions.

No.	Earthquake event	Year	Station	Earthquake magnitude	Epicentral distance (km)
1	Imperial-Vally-06	1979	Brawley Airport	6.53	10.42
2	Imperial-Vally-06	1979	EI Centro Array #4	6.53	7.05
3	Landers	1992	Lucerne	7.28	2.19
4	Menyuan	2022	62HUC	6.9	10
5	Wenchuan	2008	051MZQ	8.0	14

materials consist entirely of C35 concrete. The shear modulus of the surrounding rock is 1 GPa, and its shear density is 2200 kg/m^3. Specific material parameters are provided in Table 4. Based on this, three tunnel heights of 6, 9, and 12 m were constructed to explore the influence of tunnel clearance height on damage.

A three-dimensional (3D) finite element model (FEM) is developed in Abaqus, with its dimensions set to the prototype scale. To mitigate boundary effects in the coupled analysis of fault dislocation and seismic motion, the distance from the model boundary to the middle line was designated five times the tunnel diameter (China Merchants Chongqing Transportation Research and Design Institute Co., Ltd., 2019). For discretization, the mesh of the surrounding and tunnel utilized eight-node brick reduced integration elements (C3D8R). To determine the maximum size of the surrounding element, Eq. (6) (Kuhlemeyer & Lysmer, 1973) was utilized:

$$h_{\max} = \left(\frac{1}{10} - \frac{1}{8}\right)\lambda, \tag{6}$$

where $h_{\max}$ and λ represent the maximum element size of the surrounding rock and the shear wave length of seismic motion, respectively. In this study, pulse waves such as Menyuan wave are used as the main frequency component of input seismic motion. V_s is approximately 462.3 m/s, while $f_{\max}$ is set as 20 Hz. Therefore, the maximum element size used in this study is approximately 2.3 to 2.9 m. Additionally, in the stress concentration area of the tunnel surrounding rock, the local encrypted mesh is needed to accurately capture the plastic deformation and failure mode.

To simulate the dislocation effect of the fault plane and the contact interactions between the tunnel structure and the surrounding rock, surface-to-surface contact is defined at both the fault plane of the hanging wall and footwall, as well as the contact point between the tunnel and the surrounding rock. In the case of "face-to-face contact," the Coulomb friction law is implemented by defining the normal and tangential behaviors as "hard" and "penalty" types, respectively. The "hard" type characterizes the compressive interaction between the master and slave surfaces, allowing separation under tensile conditions. The tangential "penalty" behavior specifies the shear behavior of the two surfaces based on their contact state, employing a friction coefficient set at 0.4, derived from the internal friction angle (approximately 23.6°) of the Grade V surrounding rock in this study (Xin et al., 2024a). It is important to note that tunnel excavation can also induce tensile forces in the tunnel (Shishegaran et al., 2020c; Bigdeli et al., 2021). However, this study primarily focuses on improving the seismic resilience of tunnel lining structures after seismic events and subsequent restoration. As the first high-speed railway tunnel worldwide to experience a strong earthquake induced by fault dislocation during operation, it is reasonable to assume that construction excavation had left the tunnel lining structure in a stable state. Therefore, the effects of excavation were not considered in this study.

4.3 Seismic motion selection and input

In the analysis of tunnel structural resilience, seismic motion and different tunnel structural forms are the main influencing factors of uncertainty. Due to the fault rupture mechanism, all seismic motions contain velocity pulses in the low frequency range. Therefore, five different pulse-type seismic motions are selected as input seismic waves, and the parameters are shown in Table 5. The fragility analysis of the amplitude of the fault seismogram was carried out, and the amplitude was linearly scaled to PGA = 0.1g–1.2g, and a total of 60 seismic motion data were obtained.

The concrete constitutive model employed in this study is the concrete damage plastic model (Fig. 11)

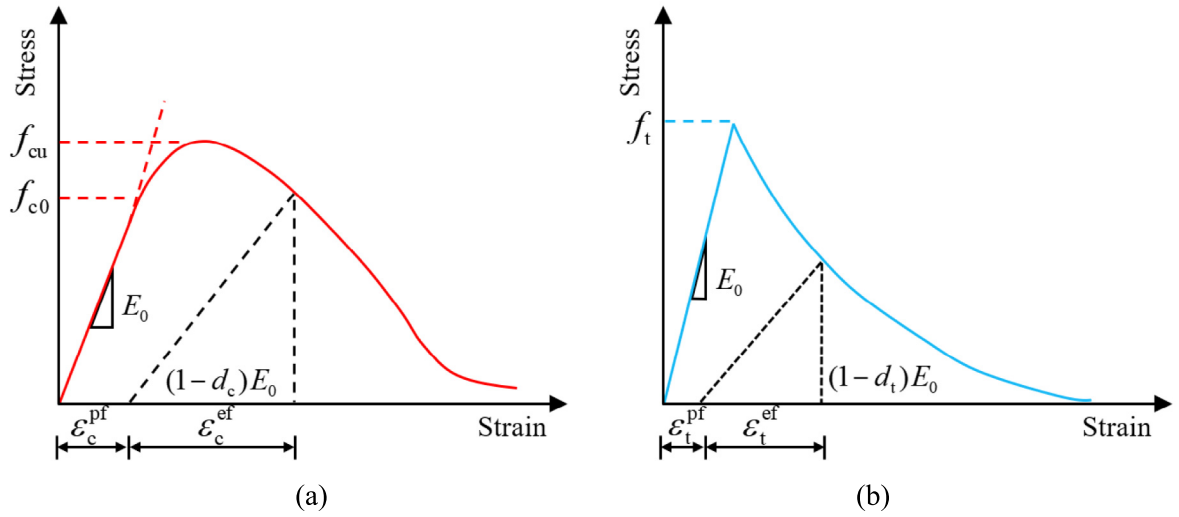

Fig. 11. Constitutive models for the concrete. (a) Under compression, and (b) under tension.

Table 6
Plastic damage parameters of concrete.

Material	Young's modulus (GPa)	Poisson's ratio, v	Dilation angle (°)	Eccentricity	f_{b0}/f_{c0}	K	Viscosity parameter
Concrete (C35)	31.5	0.2	35	0.1	1.15	0.667	0.0005

Note: K is the ratio of the second stress invariant on the tensile meridian to that on the compressive meridian at the same hydrostatic pressure.

(X. Chen et al., 2023), with specific parameters detailed in Table 6. The implementation of the dynamic analysis procedures and boundary conditions is outlined as follows:

Step 1: Ground stress balance

The initial ground stress field is a critical initial condition for the finite element analysis of the structure-foundation interaction, as the accuracy of the equilibrium result directly influences the numerical analysis results. Initially, only gravitational forces are considered in the static analysis of the finite element model. Concurrently, normal direction constraints are applied to the lateral boundary of the model, while fixed constraints in both normal and tangential directions are applied to the bottom boundary. This is accomplished using an automatic geostress balancing method in the 3D finite element software, which establishes the initial stress field for subsequent fault dislocation analysis.

Step 2: Fault dislocation application

Based on the ground stress balance, the bottom and lateral boundaries of the hanging wall are modified to apply only normal direction constraints. A 3-m displacement in the fault direction is applied to the hanging wall, following the proportional relationship of the fault dislocation. The initial stress field corresponding to the final fault dislocation is obtained, and the stress tensor for all elements, together with the reaction force (RF) at the model boundary nodes, is extracted from the computational structure.

Step 3: Application of dynamic boundary conditions

Subsequently, reasonable dynamic boundary conditions are established at the boundary nodes by replacing the fixed boundary with a viscoelastic artificial boundary. The extracted stress tensor serves as the initial stress of the elements, while the reaction force at the model boundary nodes is treated as the external load, as illustrated in Fig. 12. As the model is already in equilibrium, it indicates that all elements are under stable and constant stress.

Step 4: Application of seismic waves

Finally, the east–west Wolong seismic wave is applied along the tunnel axis. The input seismic wave is converted into equivalent node forces (ENF) at the boundary nodes, and the velocity-displacement time history data of the seismic wave is incorporated into the wave equation for calculation (Du et al., 2010; J. Huang et al., 2017).

4.4 Data preparation and generation

The initial step in employing ensemble learning methods for tunnel resilience analysis is to define the tunnel damage condition and select relevant input parameters. In this study, the damage index (DI) of the tunnel is defined as the ratio of the actual bending moment (M_{Sd}) of the tunnel section to its bearing moment (M_{Rd}). Adaboost.RT was employed to establish the relationship between the random variables and the damage indexes (M_{Sd}/M_{Rd}), thereby forming the foundation of the prediction model

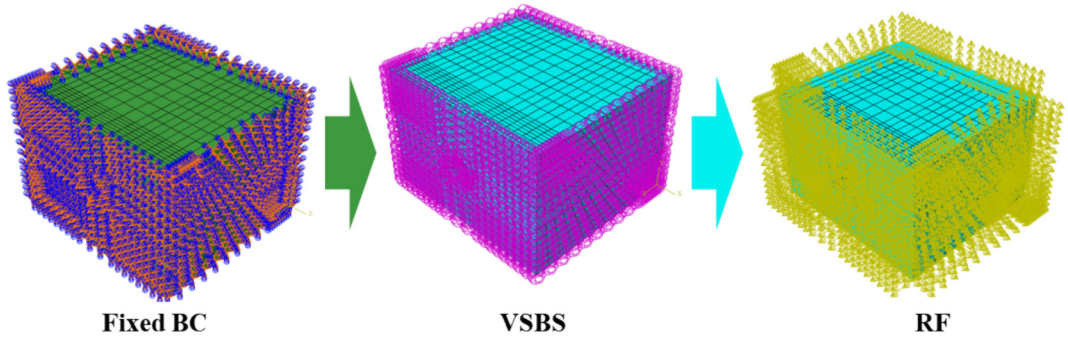

Fig. 12. FEMs for dynamic analysis: dynamic analysis procedure.

(Argyroudis et al., 2012). Data collection and preprocessing are critical in assessing the resilience of tunnel linings, primarily obtained through numerical simulations. To explore the damage mechanisms of tunnel linings under the combined effects of fault and seismic motions, three tunnel models were developed. These models varied in lining structure, peak ground motion, and seismic motion type. The simulations extracted physical parameters, such as bending moment capacity, tension and compression damage factors, stress, strain, and displacement, to investigate the mechanisms of damage and instability in tunnel linings. The damage levels in the tunnel model were categorized into five classes: no damage d_{s0}, slight damage d_{s1}, moderate damage d_{s2}, extensive damage d_{s3}, and complete damage d_{s4}. The median failure indicator, representing the central value of DI, was selected in this study for its robustness and reliability in predicting the typical failure state of the tunnel lining, providing valuable insights for engineering design and decision-making. Table 7 presents the relationship between the ranges of DI and their corresponding states (Meng et al., 2024). The database for the Adaboost. RT algorithm models is derived from damage degree values calculated during numerical simulation tests. However, due to varying units and dimensions of the input data, the ranges of different variables differ significantly, necessitating dimensionless processing of the input data. All input data are all positive; therefore, the S-type function is selected as the response function. The sample data is normalized by transforming the values to the range [0, 1], as shown in Eq. (7).

$$x^* = \frac{x - x_{\min}}{x_{\max} - x_{\min}}, \tag{7}$$

where x is the original data, $x_{\max}$ and $x_{\min}$ are the maximum and minimum values of the original data, respectively.

The input data for the model were derived from the results of the numerical simulations. First, all possible combinations of tunnel structural forms, surrounding rock shear modulus, and tunnel heights were generated using the Cartesian product method, ensuring comprehensive consideration of variable combinations. Weighted sampling was then applied, assigning a specific weight to each seismic wave based on its PGA to reflect the higher likelihood of occurrence for certain seismic waves in reality. This process ensured that seismic waves with higher probabilities were adequately represented. A total of 200 datasets were selected for model training, taking into account variables such as structural forms, peak ground acceleration, and the mechanical properties of the surrounding rock. The root mean square error (RMSE), mean absolute error (MAE), and coefficient of determination (R^2) were used to evaluate the predicted and simulated values of the sample set, as shown in Eqs. (8) to (10) (Bai et al., 2023).

$$\mathrm{MAE} = \frac{1}{n}\sum_{i=1}^{n}\left|y_i - \hat{y}_i\right|, \tag{8}$$

$$\mathrm{RMSE} = \left[\frac{1}{n}\sum_{i=1}^{n}\left(y_i - \hat{y}_i\right)^2\right]^{1/2}, \tag{9}$$

$$R^2 = 1 - \frac{\sum_{i=1}^{n}\left(y_i - \hat{y}_i\right)^2}{\sum_{i=1}^{n}\left(y_i - \bar{y}_i\right)^2}. \tag{10}$$

Table 7
Relationship between failure indicator range and failure state.

Damage state (d_s)	Range of damage index (DI)	Central value of DI
No damage d_{s0}	$M_{sd}/M_{Rd} \le 1.0$	–
Slight damage d_{s1}	$1.0 < M_{sd}/M_{Rd} \le 1.5$	1.25
Moderate damage d_{s2}	$1.5 < M_{sd}/M_{Rd} \le 2.5$	2.00
Extensive damage d_{s3}	$2.5 < M_{sd}/M_{Rd} \le 3.5$	3.00
Complete damage d_{s4}	$3.5 < M_{sd}/M_{Rd}$	–

5 Result analysis

5.1 Performing feature importance analysis

In the study of tunnel seismic fragility and resilience using ensemble learning, parameter importance analysis is essential for identifying key control factors. This analysis quantifies the marginal influence of each input parameter on the output through numerical simulations (as shown in Fig. 13), effectively identifying key factors limiting structural resilience and providing a theoretical basis for optimal design. In this study, the Adaboost.RT integrated algorithm was employed to develop a predictive model. Table 8 presents the parameter system utilized in the algorithm and its functions. The results indicate that the PGA exhibits the strongest correlation with the tunnel damage index. In tunnel engineering, PGA represents the maximum ground acceleration induced by seismic waves and directly influences the forces acting on the tunnel structure. The structural form of the tunnel (such as segmented, horseshoe, or circular) determines its stiffness and seismic performance, while the surrounding rock properties (such as strength and shear modulus) dictate the external pressure and support capacity. Additionally, the weight ratios for the tunnel lining structure, shear modulus of the surrounding rock, and the model size are 0.35, 0.18, and 0.11, respectively. This highlights that the influence of PGA on the tunnel's dynamic response is more significant than that of the tunnel structure and the mechanical properties of the surrounding rock.

Nevertheless, the tunnel's structural form significantly affects seismic damage, a factor often overlooked in previous studies. For instance, larger PGA values lead to stronger seismic dynamic loads, requiring the structural form to be sufficiently robust and well-designed to absorb seismic energy and maintain stability. At the same time, surrounding rock dimensions and mechanical properties also critically influence tunnel stability. To address these factors, the effects of surrounding rock properties and tunnel lining structure on seismic fragility and structural resilience are further discussed using detailed numerical simulation models.

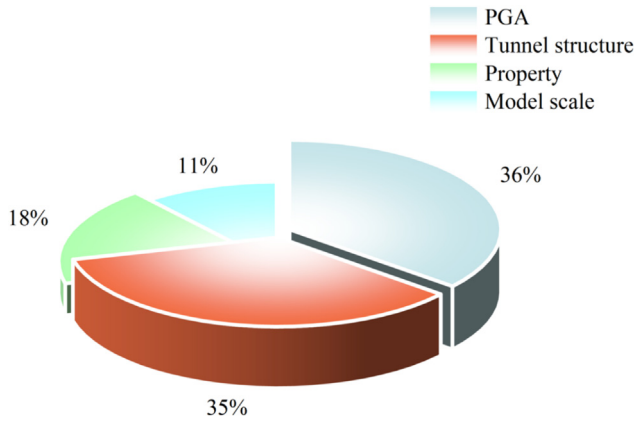

Fig. 13. Importance coefficients of parameters.

5.2 Verification of ensemble learning algorithms

To ensure model reliability and generalizability, feature selection was performed to analyze parameter correlations (as shown in Fig. 14(a)). This analysis revealed that the three primary input parameters—PGA, TS, and G_s—all exhibit correlations greater than 0.7. To further ensure model robustness, the dataset (200 samples) was randomly split 10 times, with each split generating a training set (140 samples) and a testing set (60 samples) in a 70:30 ratio. For each training set (140 samples), a 5-fold cross-validation approach was employed (see Fig. 14(b)), where in each fold, 80% of the data (112 samples) was used for training and 20% (28 samples) for validation. This approach ensured robust hyperparameter tuning and helped improve model generalization. Early stopping was applied based on the validation performance to prevent overfitting. Once the optimal hyperparameters were determined, the final model was trained on all 140 training samples, while the independent test set (60 samples) was reserved for final evaluation. As shown in Fig. 14(c), the validation loss curve stabilized within 10 training epochs, indicating effective convergence and generalizability (Harati et al., 2024).

This study employs support vector regression (SVR), the backpropagation (BP) neural network, and the extreme learning machine (ELM) as base learning models. To further evaluate the effectiveness of the proposed AdaBoost.RT model, a comparative analysis was performed against individual base prediction models (see Fig. 14(d)). In Fig. 4, the upper and lower solid lines denote the extreme absolute prediction errors of each model, while the red median line represents the 50th percentile of absolute errors (Shishegaran et al., 2021c; Cao et al., 2021). The boxplot of the AdaBoost.RT model shows the smallest area distribution among all models, indicating the highest prediction accuracy and the lowest absolute prediction error. To further enhance model training, L2 regularization was applied during training to mitigate overfitting. Moreover, a relatively small learning rate was maintained throughout training to limit the impact of weak learners, thereby preventing overfitting (Ayvaz et al., 2021).

Figure 15 illustrates the validation of the prediction model based on the Adaboost.RT algorithm. Figure 15 (a) presents the distribution plot of 10 experiments, depicting the median and variability range for both the training and test sets. The coefficients of determination for the training set and test set are 0.978 and 0.959, respectively. Notably, after each random partition, the training set undergoes cross-validation, and the model's performance metrics on the validation and test sets are recorded across 10 independent experiments (as shown in Table 9). Furthermore, the simulation results from 60 randomly selected samples in the test set were compared with the predictions obtained from the model, as shown in Fig. 15(b). The

Table 8
Adaboost.RT involves parameters and functions.

Input parameter			Output parameter	Role
Lining	Surrounding rock	Seismic motion		
Tunnel structure (TS) (such as horseshoe, circular, and shock absorbing joint)	Shear modulus (G_s)	Peak ground acceleration (PGA)	Bending moment (M)	Classification of damage grade
Strength of reinforced concrete (SRC)	Density (ρ)	Near-Fault Ground Motion (NFGM)	Deformation (U)	Quantification of structural function recovery
Thickness (H)	Model scale (MS)	–	Damage (D)	Analysis of damage mechanism

maximum error between the simulated and predicted values is 9.5%, which satisfies the requirements of the prediction model. Additionally, Fig. 15(c) compares the seismic fragility curves derived from the prediction model and numerical simulation, both of which meet the requirements of the model. This also indicates that the fragility curve of the method is consistent across all damage states. The model demonstrates high accuracy and is suitable for seismic fragility analysis of tunnels subjected to the coupling of faults and seismic motion.

5.3 Fragility analysis of tunnel structure

5.3.1 Influence of tunnel structure

The stiffness and strength characteristics of different tunnel structures vary, affecting the response of the tunnel to seismic loads and consequently altering the risk of damage. This paper analyzes the seismic fragility of high-speed railway tunnels by modifying the tunnel structures and discusses the damage effects associated with varying tunnel heights. Figure 16(b) illustrates the seismic fragility of tunnels of varying heights across different structural designs. As shown in Fig. 16(a), the damage probability of the prototype structure exceeds that of the shock-absorbing joint structure, while the circular structure exhibits the lowest damage probability. This is attributed to the circular tunnel's ability to distribute forces more uniformly under fault dislocation and seismic motion, effectively absorbing seismic wave energy and reducing damage probability. As the peak ground acceleration increases, the damage probability rises progressively. For instance, Fig. 16(b) illustrates that at a PGA of 0.6g and a tunnel height of 6 m, the probability of moderate damage for the prototype structure is 1.21 times greater than that for the circular structure. The probability of tunnel damage increases with tunnel height. This finding aligns with previous studies (Sun et al., 2024; Reddy et al., 2024). This occurs because taller tunnels may experience greater surface loads and groundwater pressures, resulting in increased loads and stresses on the tunnel structure. Additionally, taller tunnel structures are more susceptible to uneven settlement and stress concentration during repairs, exacerbating structural damage. Specifically, at a PGA of 0.6g, the probability of minor damage for a 12-m high tunnel is 1.12 times that of a 6 m high tunnel, assuming all structures are prototypes. Notably, this study's damage and failure analysis focuses on fault dislocation zones. The results show that the likelihood of widespread damage to the prototype tunnel exceeds 50% at a peak acceleration of 0.4g, with this probability increasing as peak acceleration rises.

5.3.2 Influence of shear modulus of surrounding rock

Figure 17 presents the fragility analysis of the tunnel considering various surrounding rock properties and the damage probability under different peak ground accelerations. Figure 17(a) illustrates that the shear modulus of the surrounding rock has a significant effect on the struc-

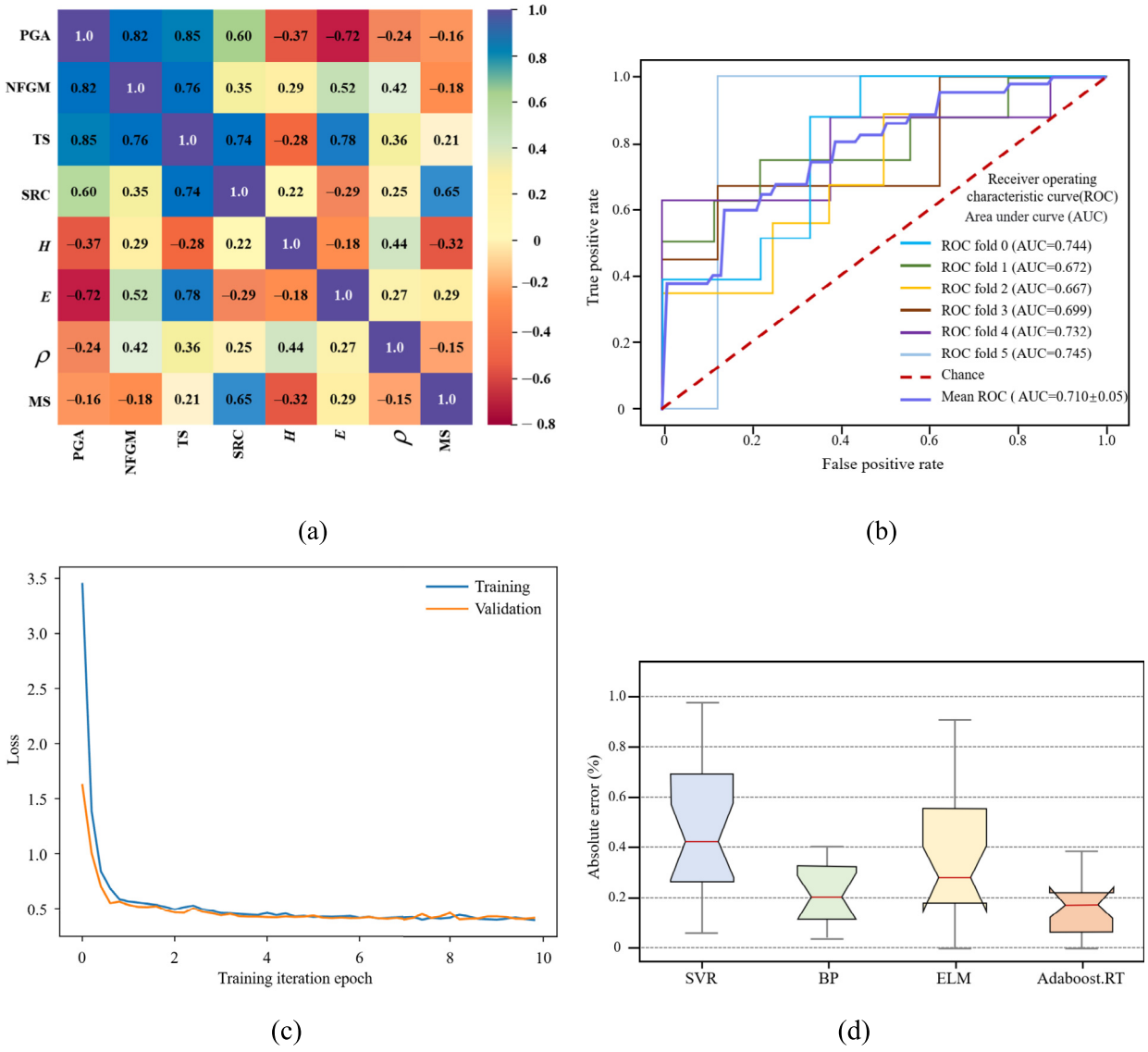

Fig. 14. Surrogate model validation. (a) Parameter correlation of each variable, (b) 5-fold cross-validation, (c) loss curve during training, and (d) absolute error between predicted and training values for each prediction model.

tural performance of the tunnel. For instance, when the PGA is 0.6*g* and the tunnel height is 6 m, the probability of moderate damage in a tunnel with a shear modulus of 1 GPa increases by 52.6% compared to that of a tunnel with a shear modulus of 6 GPa. Under the same PGA and tunnel height conditions, the probability of extensive damage in a tunnel with a shear modulus of 1 GPa is 1.88 times greater than that in a tunnel with a shear modulus of 6 GPa. This occurs because soft rock has minimal effect on tunnel performance, while seismic waves propagate more prominently in soft surrounding rock, leading to an amplification effect (Z. Chen et al., 2023). The seismic fragility characteristics of the 6 and 12 m tunnels are similar, as illustrated in Fig. 17(b). Under identical PGA and shear modulus conditions, the probability of tunnel damage increases with tunnel height. Specifically, when the shear modulus is 3 GPa and the PGA is 0.6*g*, the probability of extensive damage in a 12 m tunnel is 1.23 times that of a 6 m tunnel. When the PGA is 1.0*g*, under identical conditions, the probability of extensive damage in a 12 m tunnel increases by 9%.

5.4 Resilience analysis of tunnel structure

5.4.1 Influence of tunnel structure

Under the combined effects of fault and seismic motion, the influence of the tunnel structure on its functionality and resilience varies (see in Fig. 18). Assuming a total repair time of 120 days, Fig. 18(a) shows that the structural performance of the prototype structure is superior to that of the shock-absorbing joint structure under the same peak acceleration when subjected to the coupling effects of a strong earthquake and seismic motion prior to repair. As the peak acceleration increases, the structural performance

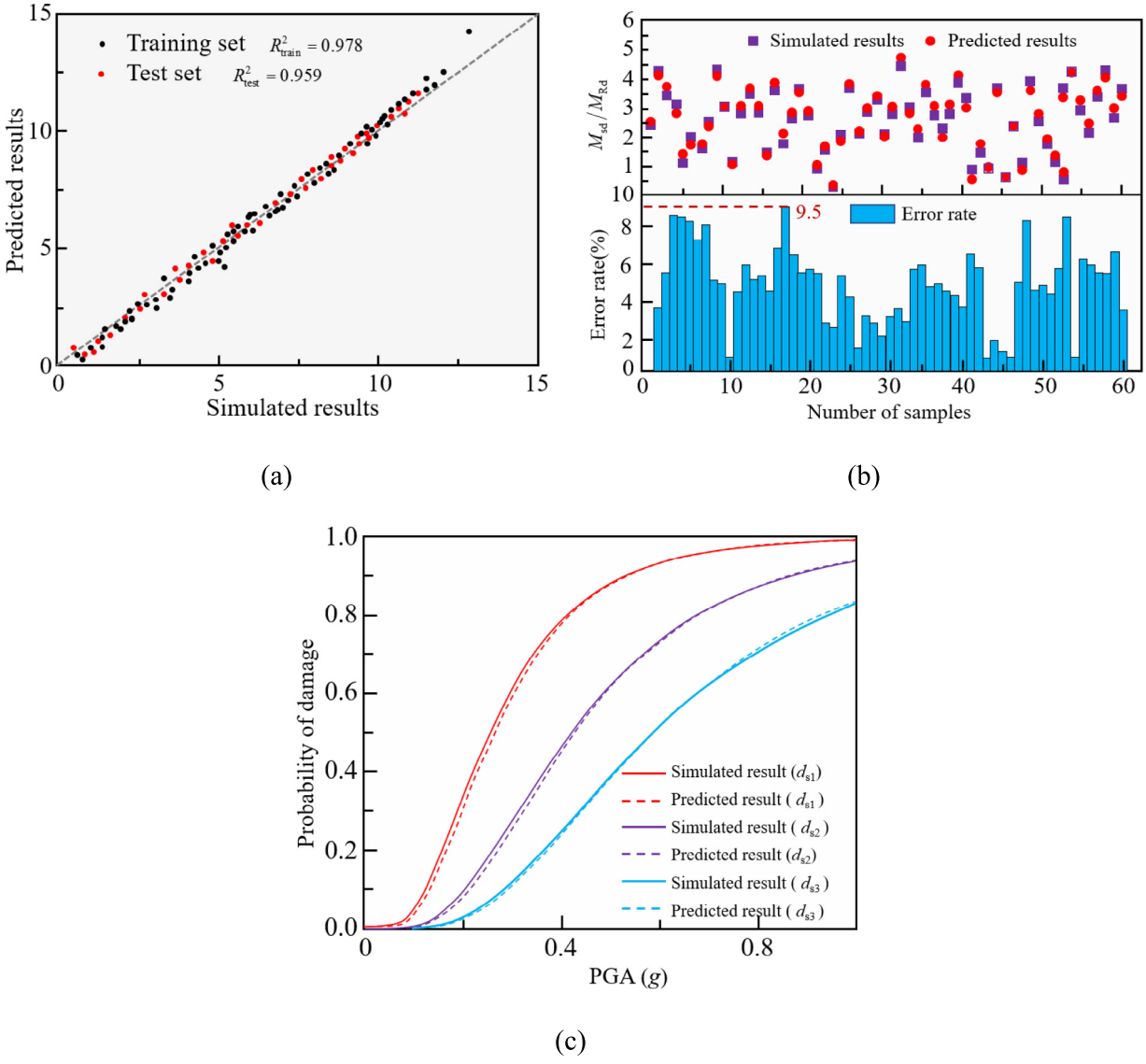

Fig. 15. Accuracy validation of the surrogate model. (a) Determination coefficient, (b) comparison of simulated and predicted values, and (c) fragility validation.

Table 9
Comparison and validation between the training set and the testing set.

Algorithms	Dataset	MAE	RMSE	R^2
Adaboost	Train	0.141	0.185	0.978
	Test	0.237	0.263	0.959

of all sections decreases significantly. Furthermore, excluding the 10 days decision time, the structural performance of the tunnel recovers after approximately 80 days. However, the functional recovery of the prototype tunnel remains slow, while the structural performance can be significantly improved by incorporating a shock-absorbing joint. Figure 18(b) presents the resilience indices of various tunnel structures after 15 days of repair, considering different peak accelerations and tunnel heights. Under low acceleration amplitudes, the tunnel functionality can reach 0.95 across different structural forms, with minimal performance differences observed among the various structures, all exhibiting high resilience. As peak acceleration increases, the performance of the tunnel structure gradually decreases. Meantime, under varying tunnel structures, performance differences become increasingly apparent. Specifically, at a peak ground acceleration of 0.4*g*, the tunnel structure exhibits high resilience as tunnel height increases, indicating that height also has minimal influence on the resilience index at lower PGAs. In addition, at a PGA of 0.8*g* and a tunnel height of 6 m, the resilience of the circular structure increases by approximately 20% compared to the prototype structure. At a PGA of 0.8*g* and a tunnel height of 12 m, the resilience of the circular structure is only 14% greater than that of the prototype structure. This indicates that increased tunnel height reduces the resilience of the tunnel

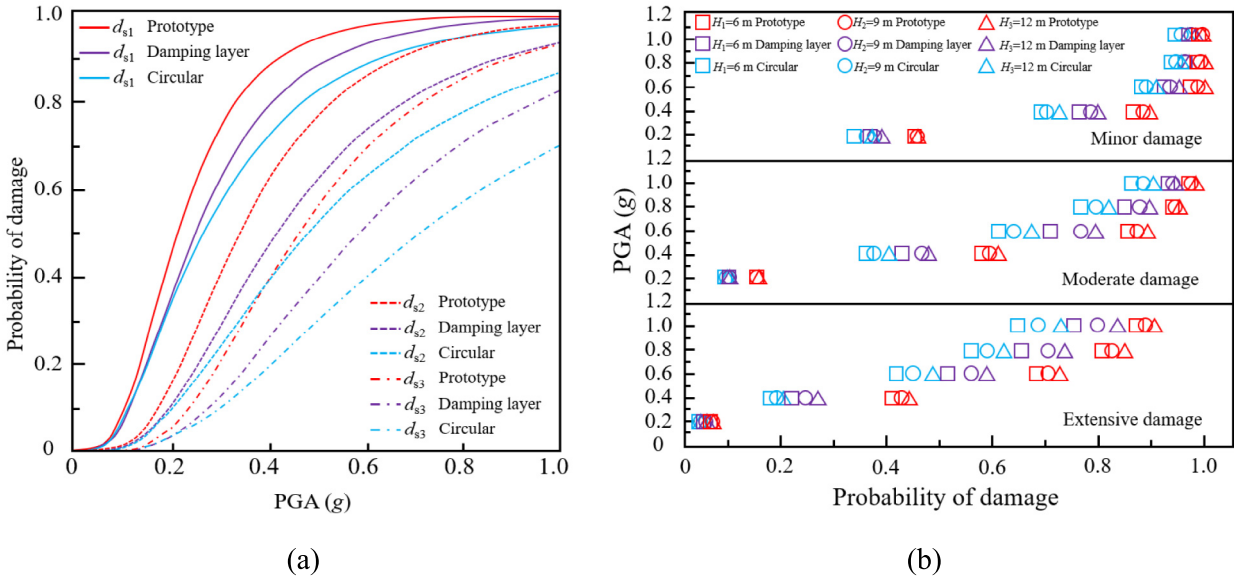

Fig. 16. Fragility curves of tunnels with different tunnel heights and construction of the surrounding rock. (a) Fragility curves, and (b) probability of damage under different PGAs.

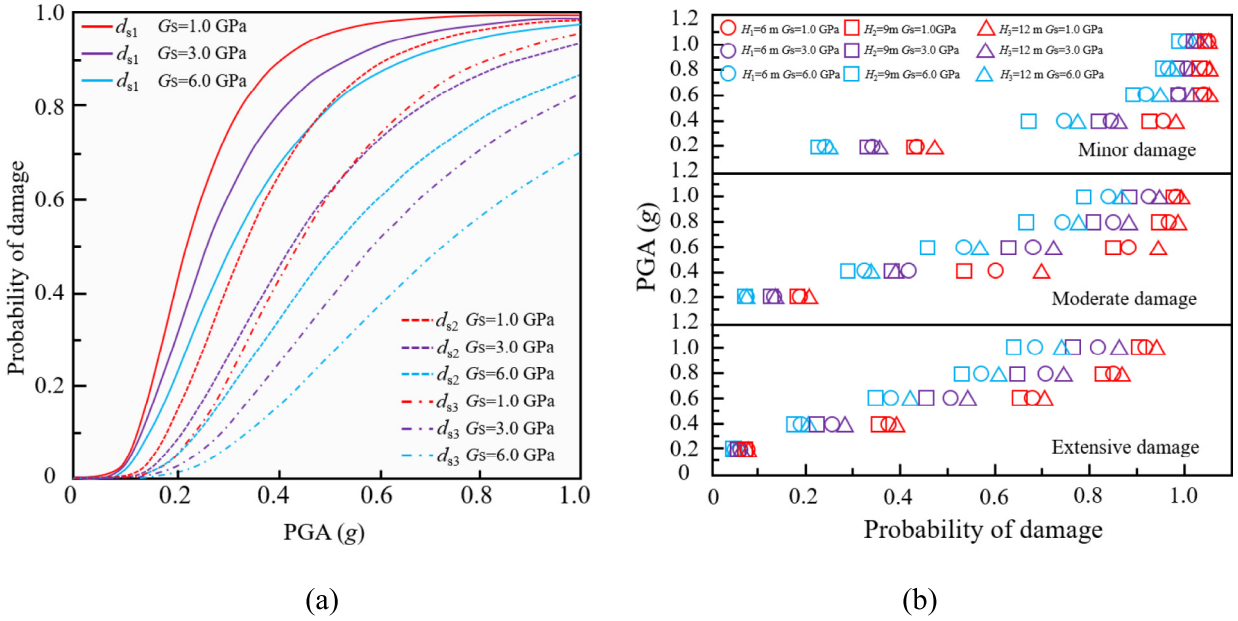

Fig. 17. Fragility curves of tunnels with different tunnel heights and shear modulus of the surrounding rock. (a) Fragility curves, and (b) probability of damage under different PGAs.

lining. With a PGA of 1.2*g* and a tunnel height of 6 m, the resilience of the circular structure is 12% higher than that of the prototype structure. This further indicates that the resilience of the tunnel structure decreases more significantly as the peak acceleration increases.

5.4.2 *Influence of shear modulus of surrounding rock*

Figure 19 illustrates how the shear modulus of the surrounding rock affects the structural performance and resilience of the tunnel under the combined influence of active fault dislocation and seismic motion. In Fig. 19(a), the results indicate that the performance of the tunnel structure decreases as the shear modulus of the surrounding rock decreases under the same peak acceleration conditions. Before the implementation of repair measures, it is clear that a higher shear modulus leads to better structural performance of the tunnel after a disaster. This indicates that when the tunnel is embedded in softer rock, the earthquake damage is more severe under the same peak ground acceleration, leading to slower functional recovery.

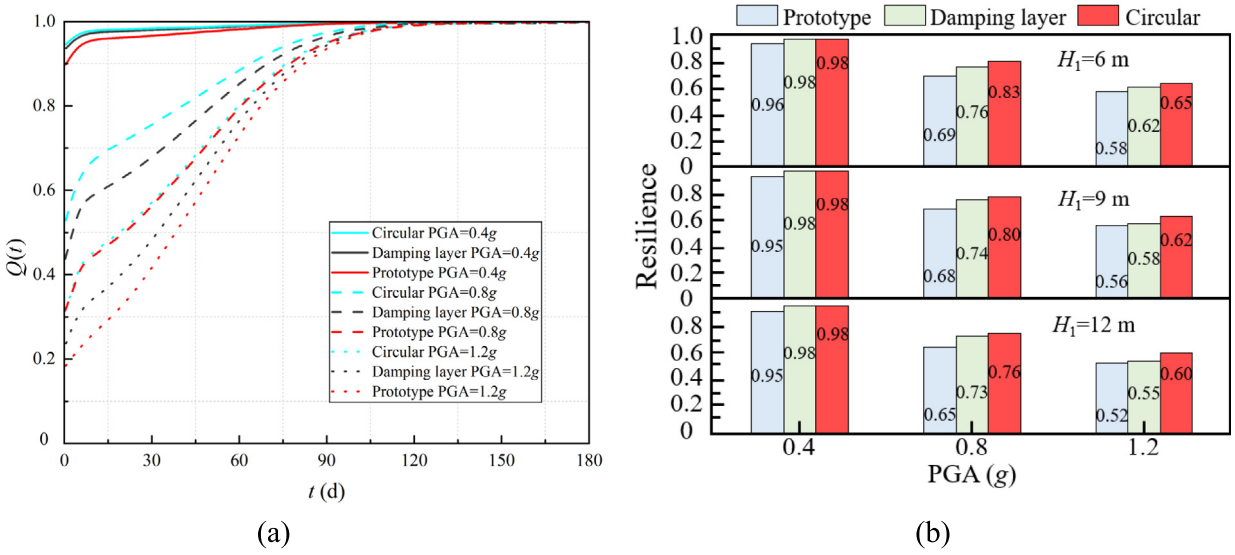

(a) (b)

Fig. 18. (a) Functionality and (b) resilience of tunnels under different construction.

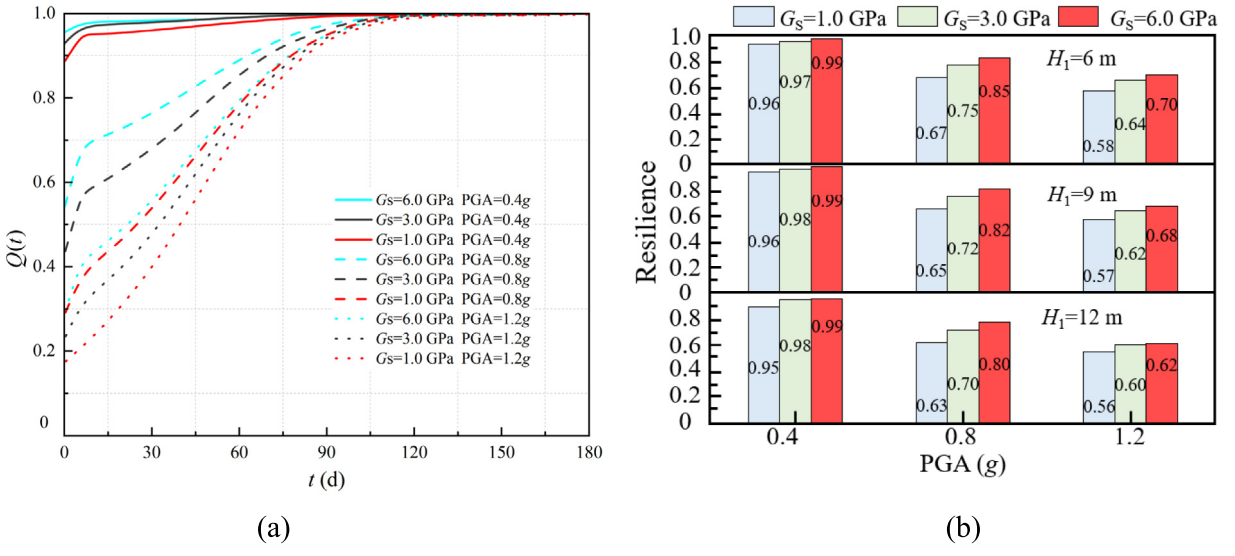

(a) (b)

Fig. 19. (a) Functionality and (b) resilience of tunnels under different shear modulus.

Figure 19(b) illustrates that, similar to the effects of tunnel structural form, the difference in shear modulus among various surrounding rocks first increases and then decreases with rising peak acceleration. Specifically, for a 9 m high tunnel subjected to a seismic intensity of 0.8*g*, the tunnel structural resilience after 15 days of repair is measured at 0.65, 0.72, and 0.82 for shear modulus of 1, 3, and 6 GPa, respectively, belonging to moderate resilience. Furthermore, at a PGA of 0.8*g*, the resilience of the tunnel with a shear modulus of 6 GPa and a height of 9 m is 26% greater than that of the tunnel with a shear modulus of 1 GPa. At a PGA of 1.2*g* and a shear modulus of 6 GPa, the resilience of the 6 m high tunnel is 1.21 times that of the 1 GPa tunnel. However, under identical conditions, the resilience of the 12 m high tunnel increased by only 11.1%. This suggests that the influence of shear modulus on tunnel resilience is also dependent on tunnel height. Additionally, comparing with Fig. 18(b), it is evident that under the excitation condition of a 1.2*g* peak acceleration, the influence of tunnel structure on resilience surpasses that of the surrounding rock's shear modulus at the same tunnel height, which aligns with the findings from the fragility analysis ratio.

6 Discussion

6.1 Analysis of seismic mechanism of different repair measures of crossing-fault tunnel

Tunnels are susceptible to various types of structural damage stemming from the combined influences of seismic faults and seismic motions. This study leverages numerical

simulations to elucidate the damage mechanisms impacting various tunnel structures under the dual influence of active faults and seismic motions. It is essential to understand how fault activity, seismic wave propagation, and the deformation of surrounding rock contribute to tunnel structure vulnerability. Additionally, this analysis aims to identify the damage characteristics of tunnels subjected to different repair measures, facilitating a deeper understanding of the dynamic interactions between the tunnel and surrounding geological formations. By comparing the effectiveness of various repair strategies, the study assesses their mitigation effects on tunnel structures, particularly focusing on how they interact with the combined influences of fault activity and seismic motions. The strengths and weaknesses of each repair strategy are critically evaluated to identify the most beneficial approach. The seismic resilience enhancement mechanism of tunnel lining with the purpose of "anti-seismic and dislocation reduction, load transfer and damage limitation" is proposed and verified by the seismic resilience assessment framework, which provides a theoretical basis for seismic fortification of tunnel engineering. Figure 20 illustrates the compressive and

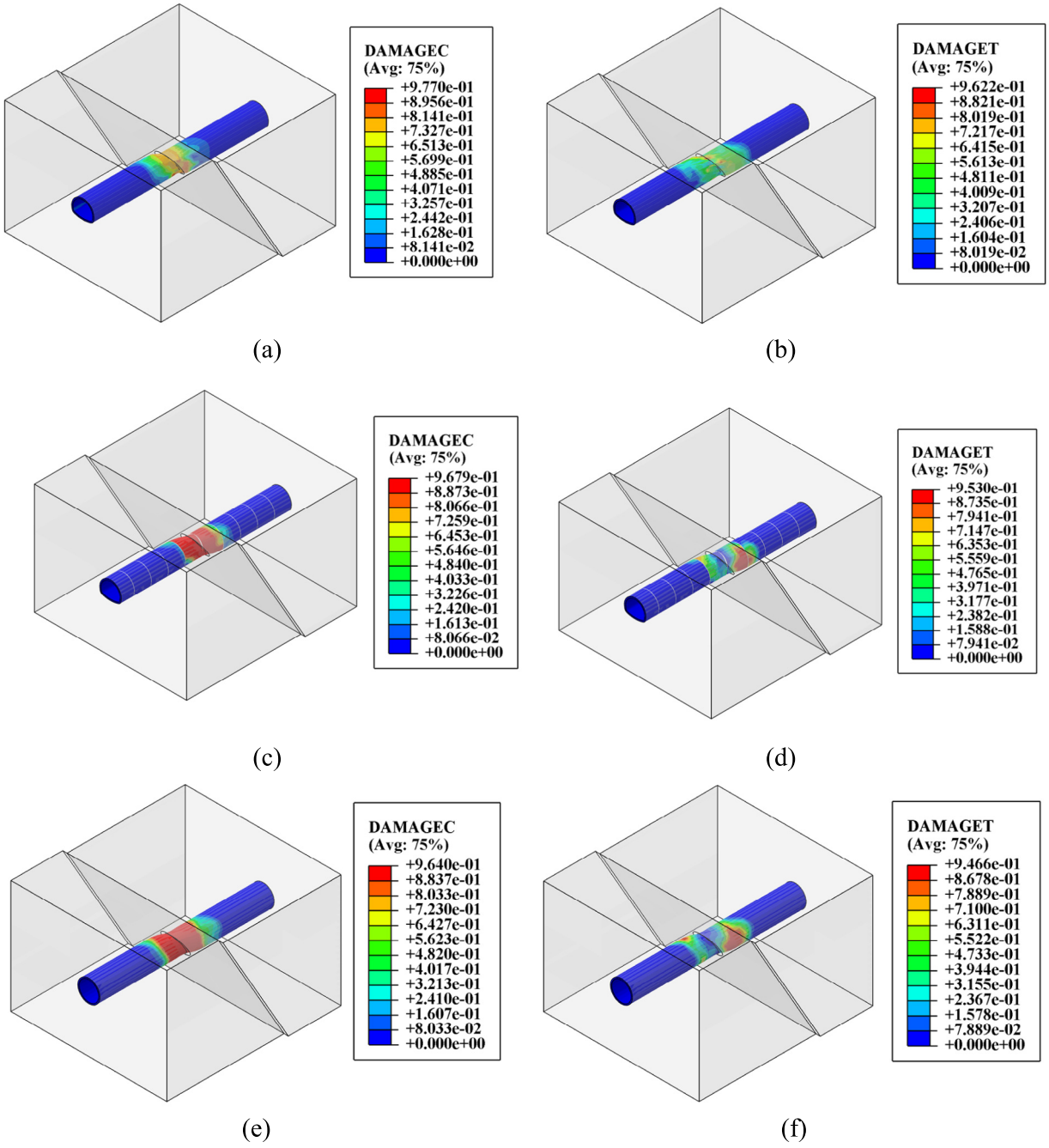

Fig. 20. Comparison of tunnel structural damage with different repair measures. (a) Prototype tunnel damagec, (b) prototype tunnel damaget, (c) shock-absorbing joint damagec, (d) shock-absorbing joint damaget, (e) circular tunnel damagec, and (f) circular tunnel damaget.

tensile damage to the tunnel structure resulting from the combined effects of fault dislocation and seismic motion, as well as the influence of two different repair measures.

Figure 20 illustrates that, under the coupling effects of fault dislocation and seismic motion, the compressive and tensile damage to the prototype tunnel is most severe, while the damage to the shock-absorbing joint and circular tunnel is significantly reduced under the same conditions. Notably, the damage range of the circular tunnel is greater than that of the shock-absorbing joint, because the shock-absorbing joint has a relatively low stiffness compared to the tunnel lining. Moreover, the shock-absorbing joint retains satisfactory deformation capacity and resilience, allowing the displacement and deformation resulting from the coupling of fault dislocation and seismic motion to be concentrated at the fault. This creates a blocking effect on the hanging wall and footwall. Consequently, energy transfer at the fracture is hindered, thereby reducing the damage area. Additionally, the plastic strain magnitude (PEMAG) directly reflects the plastic deformation and damage evolution process of the landslide. Figure 21 indicates that the stress on the shock-absorbing joint at the fault is significant, further demonstrating that the shock-absorbing joint effectively reduces stress transfer.

As can be seen from Fig. 22, the tunnel structural damage in the affected section of the fault can be effectively reduced by applying shock-absorbing joints on the basis of the prototype and changing the tunnel structure to a circular shape. Specifically, for applying shock-absorbing joints, the damage factor dc is reduced by 0.933% and the damage factor dt is reduced by 0.956%. This is because the shock-absorbing joint material has a certain resilience, and the uniform layout of the entire longitudinal section improves the overall deformation ability of the tunnel, thereby improving the overall resilience of the structure. For the circular structure, the damage factor dc is reduced by 1.33%, and the damage factor dt is reduced by 1.621%. This is because the circular tunnel structure is characterized by its uniform stress distribution, superior seismic performance, and overall stability (G. Chen et al., 2024; Tsinidis et al., 2024b). In addition, compared with the tunnel structure with a shock-absorbing joint, the circular tunnel structure can mitigate the damage caused by the coupling of fault dislocation and seismic motion. At the same time, for the tensile damage, it can be observed that the shock-absorbing joint and the circular tunnel structure can effectively alleviate the tensile damage of the tunnel structure. This is because the damping joint reduces the transmission of seismic waves by absorbing and dispersing stress. The circular tunnel structure, by virtue of its uniform stress characteristics, can effectively reduce the stress concentration and reduce the tensile damage of the tunnel structure. It is worth mentioning that it can be obviously observed that the compressive damage of the tunnel structure is mainly concentrated in the fault-affected section, while the damage of the circular structure and the shock-absorbing joint structure is significantly reduced at the fault.

Figure 23 illustrates the deformation and displacement of the circular tunnel and prototype tunnel structures at various sections under the coupling effects of fault dislocation and seismic motion. The displacement and deformation of the circular tunnel are clearly more uniform than those of the prototype tunnel. Furthermore, as illustrated in Fig. 24(a) and (b), the resistance stress in the circular section is uniformly distributed perpendicular to its surface,

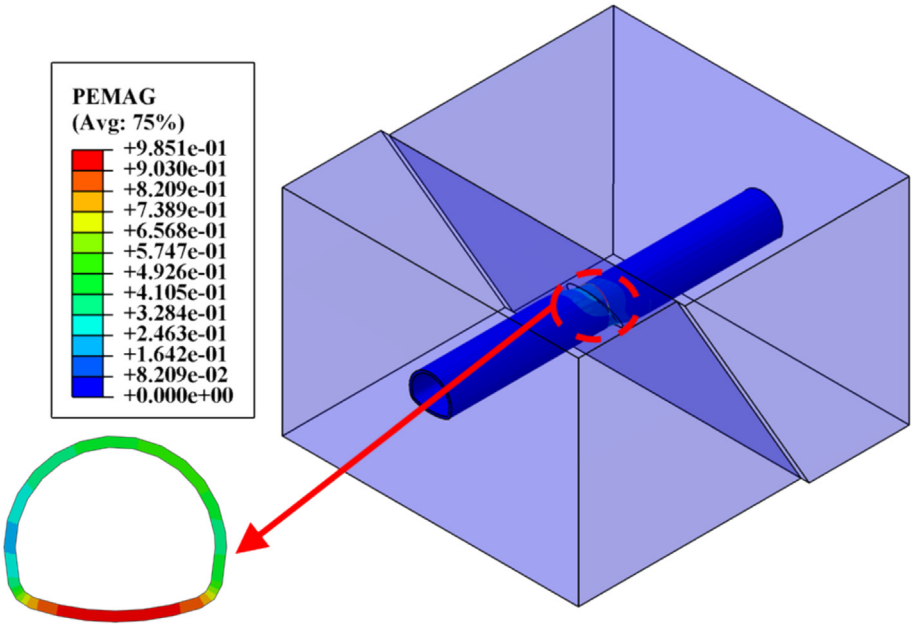

Fig. 21. Stress distribution at the fault of the tunnel structure with seismic expansion joints.

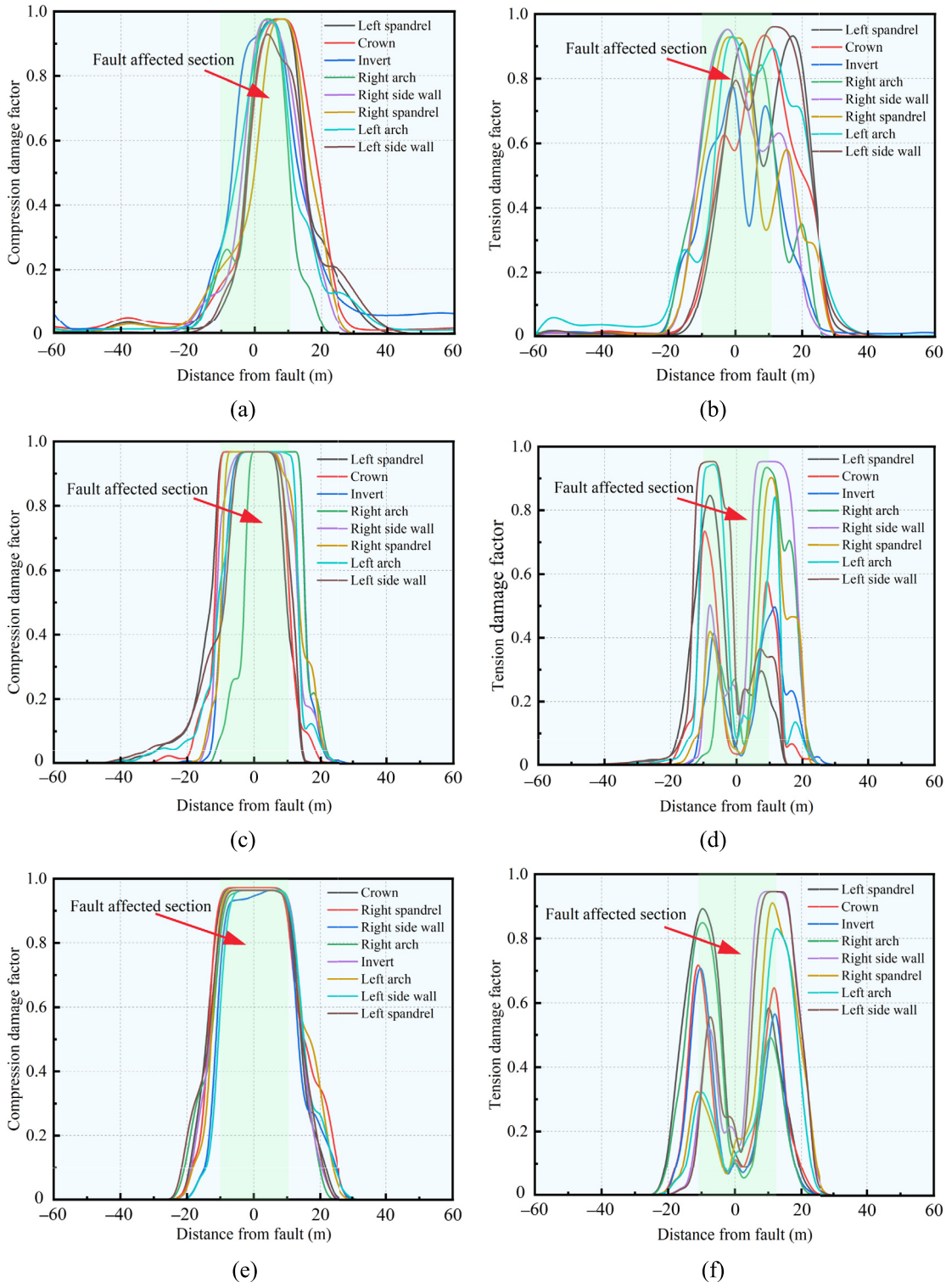

Fig. 22. Comparison of tensile and compressive damage across different tunnel structures. (a) Prototype tunnel damagec, (b) prototype tunnel damaget, (c) shock-absorbing joint damagec, (d) shock-absorbing joint damaget, (e) circular tunnel damagec, and (f) circular tunnel damaget.

whereas the maximum principal stress in the horseshoe section exhibits multiple components and stress deflection, resulting in uneven deformation. This further indicates that the circular section exhibits greater anti-seismic performance compared to the horseshoe section tunnel lining.

6.2 Seismic damage characteristics and resilience evaluation of tunnel

Highway tunnels and high-speed railway tunnels primarily exhibit five types of damage: lining cracks, lining

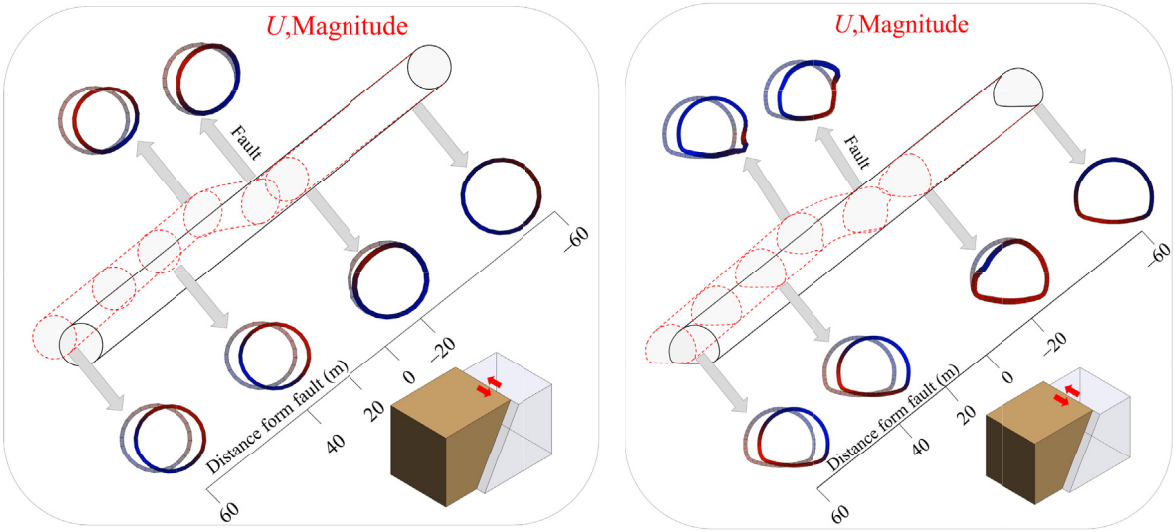

(a) (b)

Fig. 23. Displacement deformation under the coupling effects of fault displacement and seismic motion for different cross-sectional forms. (a) Circular tunnel, and (b) horseshoe tunnel.

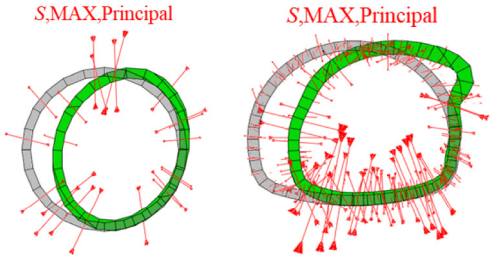

(a) (b)

Fig. 24. Stress distribution and deformation characteristics at the fault under the coupling effects of fault displacement and seismic motion for different cross-sectional forms. (a) Circular tunnel, and (b) horseshoe tunnel.

spalling, construction joint damage, pavement and underlying structure damage, and water leakage. The degree of damage may vary significantly due to changes in seismic intensity, coupling of fault dislocation, geological conditions, structure forms, and potential construction defects (Xin et al., 2024b; Huang et al., 2024). In the presence of seismic activity, the coupling effect of fault dislocation and seismic motion exacerbates the damage. The relative displacement at the fault zone, combined with the propagation of seismic waves, amplifies the stresses on the tunnel lining. This interaction increases the risk of failure, leading to a significant reduction in the tunnel's seismic resilience (Yu et al., 2016).

Moreover, fault-induced earthquakes release energy associated with the fracture of the rock mass, which generates deformations in the displacement field. The energy released from fault rupture is considerably greater than that of distant seismic events. Most seismic motions associated with fault activity are classified as near-fault pulse motions, which tend to result in more severe damage compared to distant earthquakes (Zhong et al., 2020). Consequently, fault dislocation alters the mechanical environment surrounding the tunnel, significantly affecting the structural stability and seismic resistance of the tunnel lining. Therefore, in the case of Daliang tunnels affected by seismogenic faults, the interaction between fault dislocation and strong seismic coupling has resulted in more severe damage to the tunnel lining. An investigation of the damage to the Daliang tunnel following the earthquake categorized the damage into five types: complete damage, extensive damage, moderate damage, slight damage, and no damage. Specifically, as follows:

(1) The segment of complete damage

The segment from K1971+341 to K1971+691 (350 m) experienced severe bulging of the track bed, with amplitudes reaching 30–50 cm, resulting in general damage and deformation of the track. The ditch covers on both sides are squeezed and uplifted, causing the side walls of the ditch to incline, resulting in noticeable localized damage. Damage at the fault position was particularly severe. Circumferential extrusion failure occurred in the lining, exposing the waterproof layer, with extensive spalling of the arch and deformation, fracture, and exposure of numerous steel bars, as shown in Fig. 25. The misalignment of the right wall is at K1971+394.9, while the left wall is misaligned at K1971+404.1. The horizontal dislocation is approximately 1.5 to 1.8 m, the vertical dislocation is about 0.2 to 0.7 m, and the crack width ranges from 0.3 to 0.8 m.

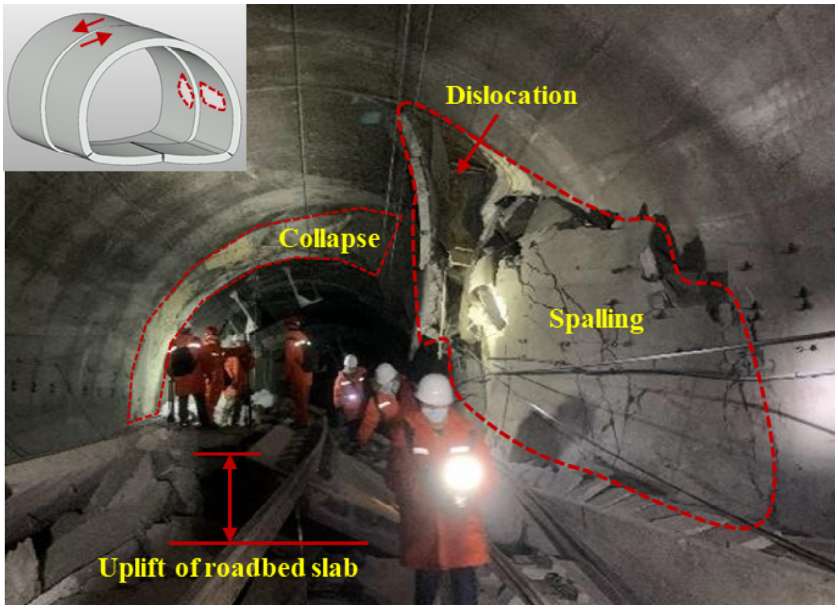

(a)

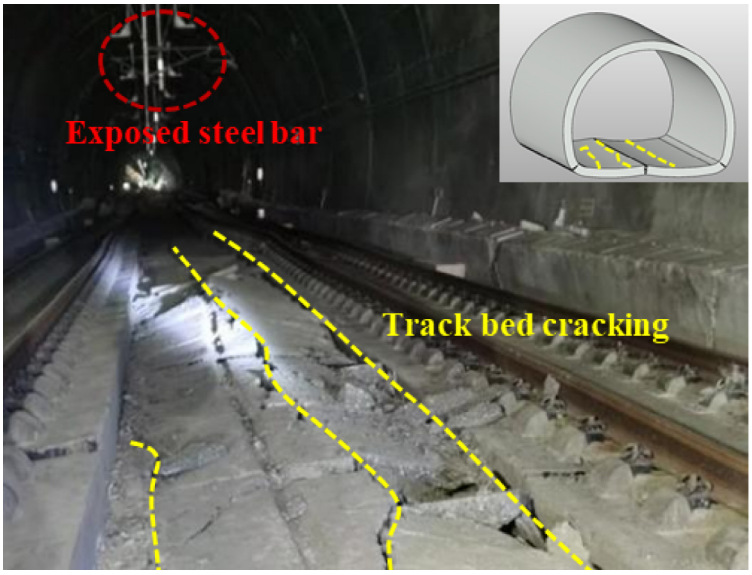

(b)

Fig. 25. Site earthquake damage in the completely damaged section of Daliang tunnel. (a) Obvious dislocations and blockages in the lining section, and (b) severe uplift and widespread cracking of the roadbed plate.

The intersection angle with the tunnel is approximately 50°, indicating primarily left lateral slip with a thrust component.

(2) The segment of extensive damage

In the extensively damaged areas, there has been an improvement in the extent of damage observed. The main manifestations include significant spalling or severe cracking of the lining, notable breakage, and exposure or even bending of the steel bar, as shown in Fig. 26. Nevertheless, the overall functionality remains compromised, with more severe structural damage, resulting in the interruption of railway service along the line. Statistical analysis indicates that there are 10 severely damaged sections with spalling blocks, each measuring between 1.5 and 10 m in length and ranging from 0.5 to 15 m^2 in area. Some of the fallen steel bars exhibit leakage, deformation, and bending, with most located within a 500-m influence range on either side of the severely affected earthquake section. Additionally, a total of 15 sections of the lining sustained serious damage due to cracks, including oblique and circumferential through cracks, as well as multiple parallel cracks intersecting in various directions. Certain sections of the lining

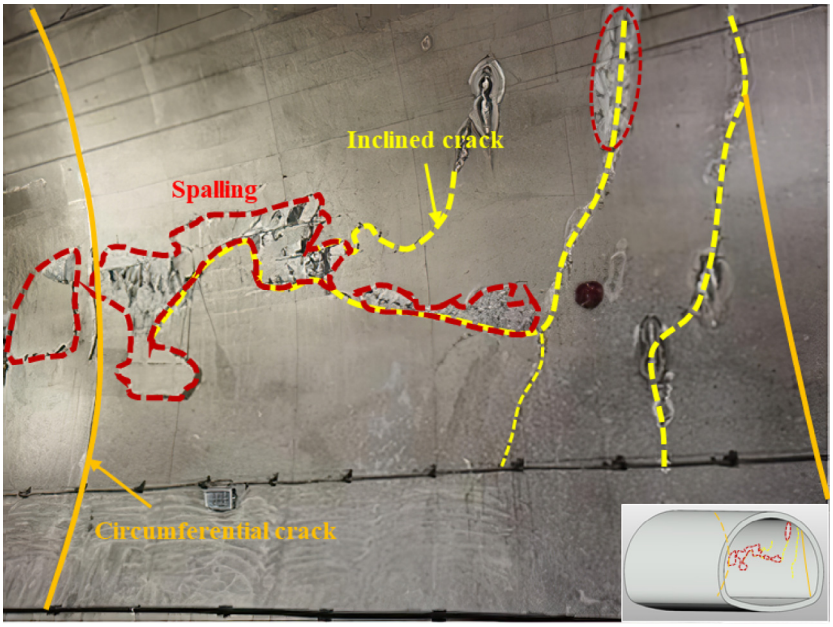

(a)

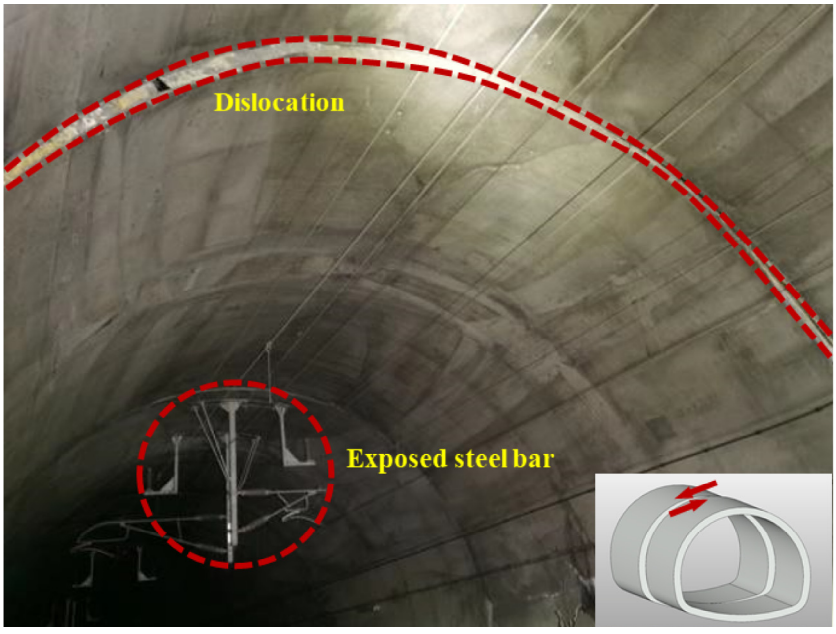

(b)

Fig. 26. Site earthquake damage of the extensively damaged section of Daliang tunnel. (a) Construction joints exhibiting cracks and spalling, and (b) lining dislocations with exposed steel bar.

structure exhibit significant compressive deformation, cracking, and dislocation.

(3) The segment of moderate damage

The primary issues in the moderate damage segment include: cracks in the side walls (primarily circumferential cracks), cracks in the invert filling layer, leakage, cracks and leaks in the adjoining cavern, blockage of the central ditch, and spalling of construction joints (see Fig. 27). These issues are unevenly distributed throughout the tunnel. The degree of damage decreases with increasing distance from the Lenglongling fault zone (LLLF). Although the overall functionality has largely been maintained, the visible structural damage poses a risk to train operations.

(4) The segment of slight damage

This section of the lining primarily exhibits localized slight cracking, minor spalling, and small falling fragments. The construction joint displays minor cracks, along with a

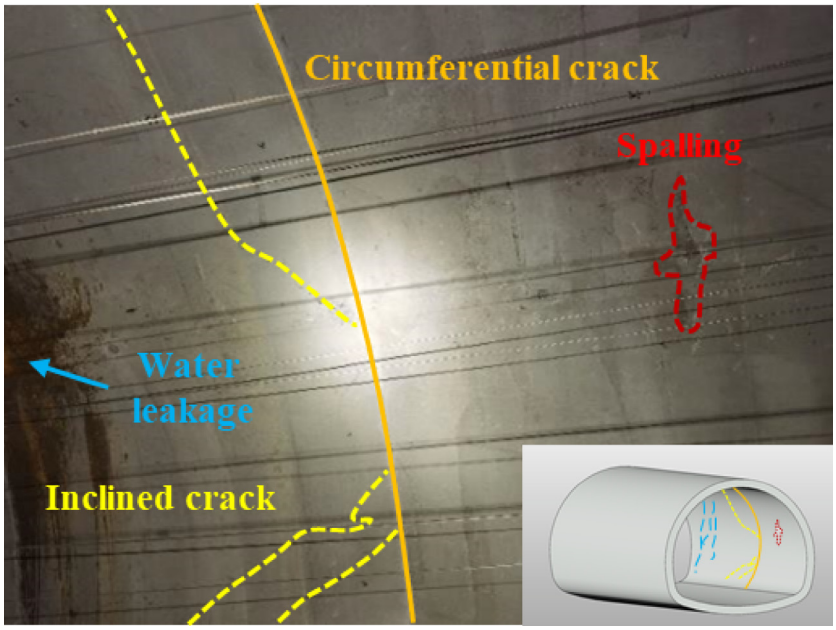

(a)

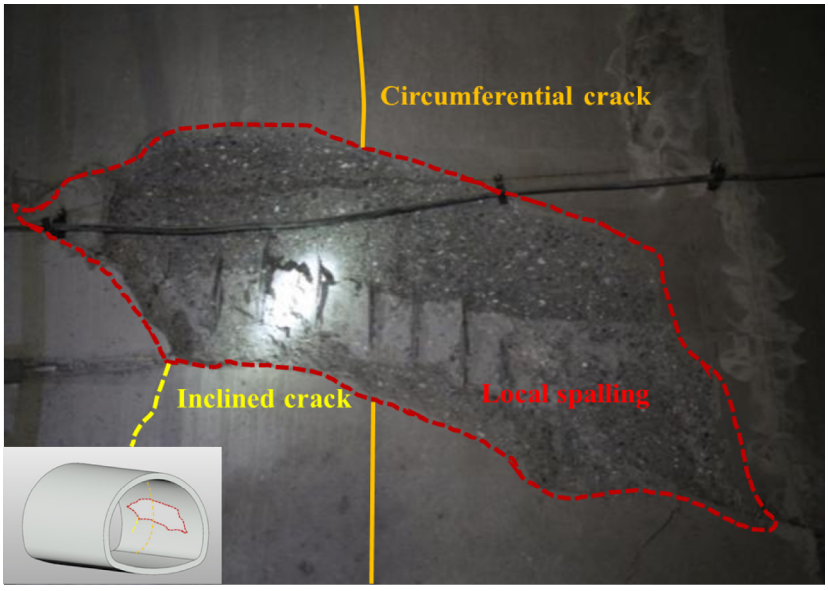

(b)

Fig. 27. Site earthquake damage in the moderately damaged section of the Daliang tunnel. (a) A few cracks and water leaks in the side walls, and (b) peeling concrete blocks, exposed rebar, and deformation.

few scattered fractures (as shown in Fig. 28). Despite this damage, the structure remains largely intact, and there is no significant influence on the safety of train operations.

Based on the research results and damage cases reported in previous earthquakes (Alliance et al., 2001), Table 10 summarizes the potential damage modes of the Daliang tunnel under different damage states. Field investigations reveal that the tunnel lining at K1971+400, which suffered severe earthquake damage, exhibits the largest dislocation. The horizontal dislocation on both sides ranges from 1.1 to 1.7 m, while the vertical dislocation ranges from 0.2 to 0.7 m. The circumferential through-crack caused by the lining dislocation measures approximately 300 to 800 mm in width and 25.2 m in length, categorizing it as an extensive damage stage. This is consistent with the conclusions obtained from the numerical simulation of the fault using the M_{Sd}/M_{Rd} method. The effectiveness of the numerical simulation is further demonstrated.

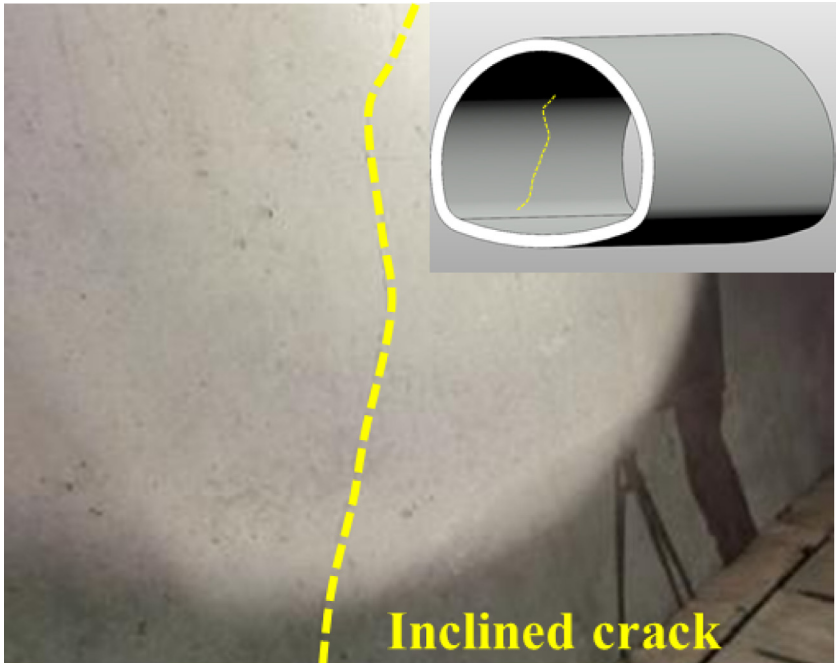

(a)

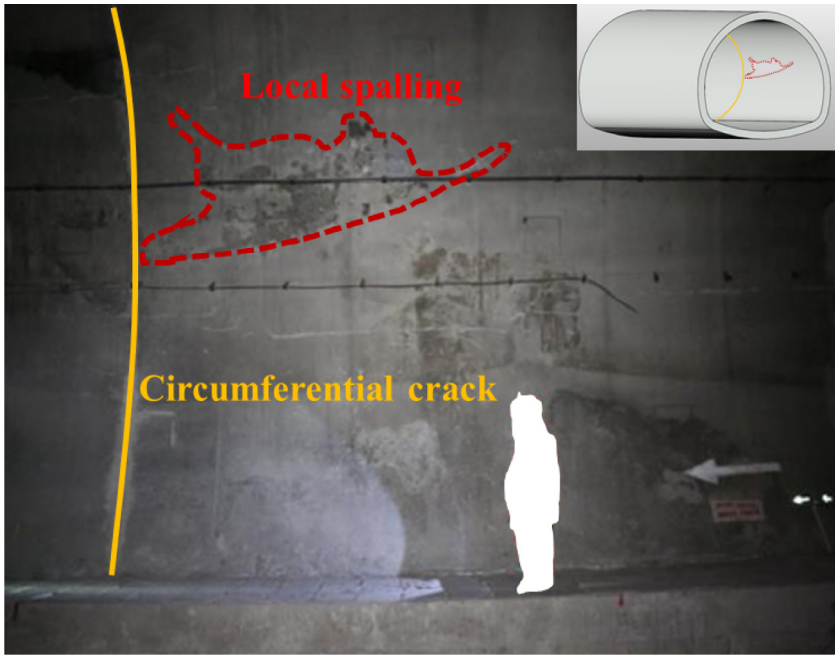

(b)

Fig. 28. Site earthquake damage in the slightly damaged section of the Daliang tunnel. (a) Localized cracks in the side walls, and (b) localized spalling and cracks in the side walls.

7 Conclusions

This paper proposes an ensemble learning approach to establish a rapid resilience assessment framework for crossing-fault high-speed railway tunnels. Employing numerical simulation methods, the study efficiently collects data on the coupling effects of fault dislocation and seismic motion. The convergence of the lining is selected as the structural performance index, with the damage index derived from the established prediction model. This approach significantly reduces the computational load for seismic fragility and resilience analyses of the tunnel

Table 10
Potential damage modes under different damage states.

Tunnel damage state	Tunnel lining	Crack specification	
		Length (m)	Width (mm)
No damage	–	–	–
Minor damage	Minor cracking and spalling	<5	<3
Moderate damage	Small cracking, spalling, and falling	5–10	3–30
Extensive damage	Large cracking, spalling, and falling	>10	>30
Complete damage	Complete collapse	–	–

structure. Field investigations from the Daliang tunnel validate the numerical simulation's accuracy. The findings are as follows:

(1) The rationality of the proposed ensemble learning algorithm and the accuracy of the prediction model have been effectively verified. The test set showed a coefficient of determination of 0.959, a root mean square error of 0.263, and a mean absolute error of 0.237, with a maximum error of 9.5%. The results of the numerical simulation closely align with the fragility curves obtained from the prediction model, further confirming the validity of the model. Additionally, the study examines the relationship between various input variables, including structure form, shear modulus of surrounding rock, tunnel height, and peak ground acceleration, as well as the output variables, such as the bending moment of the tunnel section and the convergence of the lining.
(2) The fragility importance analysis indicates that the influence of the PGA on the dynamic response of the tunnel is more significant than that of the structural design of the tunnel and the mechanical properties of the surrounding rock. Variations in the tunnel structure form, shear modulus of the surrounding rock, tunnel height, and PGA reveal that the resilience of the circular structure tunnel surpasses that of the other structural forms, with the prototype tunnel showing the least resilience. As the shear modulus of the surrounding rock increases, the resilience of the tunnel structure improves incrementally. However, as PGA and tunnel height increase, the tunnel structure sustains more damage, leading to a progressive decline in structural resilience.
(3) Numerical simulations reveal that the area of the tunnel most severely affected by damage, under the combined influence of active fault and seismic motion, is predominantly located in the fault-affected section. Variations in the structural form of the tunnel demonstrate that the prototype structure experiences the most significant damage, whereas the circular structure sustains the least damage. This finding corroborates the accuracy of the fragility and resilience analysis. Additionally, the introduction of a shock-absorbing joint substantially reduces the extent of damage across the tunnel when subjected to the coupling effects of fault activity and seismic motion.
(4) The resilience index of the tunnel lining is calculated according to the established multi-stage resilience analysis model. The convergence of the tunnel diameter is chosen as the structural resilience index, and the ratio of the actual bending moment of the tunnel section to the bearing capacity bending moment serves as the damage index. Resilience evaluations from various numerical simulations suggest that the tunnel lining exhibits high resilience under lower amplitude conditions. However, as tunnel acceleration increases, resilience decreases from high to medium. Under extreme conditions, such as with the prototype tunnel structure and a surrounding rock shear modulus of 1 GPa, tunnel resilience progressively declines from high to medium and then to low.

Data availability

The code developed in this study and sample data can be accessed from the GitHub repository: https://github.com/wangzhao0217/AdaBoost.RT_for_resilience-evaluation_of_high-speed_railway_tunnels. The data are provided under the Open Data Commons Attribution License.

CRediT authorship contribution statement

Lianjie Yang: Supervision, Project administration, Methodology, Investigation, Funding acquisition. **Chunlei Xin:** Writing – original draft. **Zhao Wang:** Writing – original draft, Methodology, Formal analysis, Data curation. **Xinyuan Yu:** Visualization, Methodology, Formal analysis. **Iman Hajirasouliha:** Writing – review & editing, Methodology. **Wenkai Feng:** Funding acquisition.

Declaration of competing interest

The authors declare that they have no known competing financial interests or personal relationships that could have appeared to influence the work reported in this paper.

Acknowledgement

This research was supported by the National Natural Science Foundation of China (Grant No. 52108361), the Sichuan Science and Technology Program of China (Grant Nos. 25CXCY0063 and 2024ZYD0154), and the State Key Laboratory of Geohazard Prevention and Geoenvironment Protection Independent Research Project (Grant No. SKLGP2022Z015).

References

Adoko, A. C., Jiao, Y. Y., Wu, L., Wang, H., & Wang, Z. H. (2013). Predicting tunnel convergence using multivariate adaptive regression spline and artificial neural network. *Tunnelling and Underground Space Technology, 38*, 368–376.

Alliance, A. L. (2001). Seismic fragility formulations for water systems: Part 1-guideline. *American Society of Civil Engineers-FEMA*.

Argyroudis, S. A., & Pitilakis, K. D. (2012). Seismic fragility curves of shallow tunnels in alluvial deposits. *Soil Dynamics and Earthquake Engineering, 35*, 1–12.

Argyroudis, S. A., Mitoulis, S. A., Hofer, L., Zanini, M. A., Tubaldi, E., & Frangopol, D. M. (2020). Resilience assessment framework for critical infrastructure in a multi-hazard environment: Case study on transport assets. *Science of the Total Environment, 714*.

Aydan, Ö., Malistani, N., Ulusay, R., & Kumsar, H. (2024). The damage and response of some underground structures by the 2023 February 6 great Turkish earthquakes and some considerations. *Engineering Geology, 336*, 107549.

Ayvaz, S., & Alpay, K. (2021). Predictive maintenance system for production lines in manufacturing: A machine learning approach using IoT data in real-time. *Expert Systems with Applications, 173*, 114598.

Bai, X. D., Cheng, W. C., Wu, B., Li, G., & Ong, D. E. L. (2023). Shield machine position prediction and anomaly detection during tunnelling in loess region using ensemble and deep learning algorithms. *Acta Geotechnica, 18*(11), 6175–6199.

Bao, F., Zeng, X. F., Lin, R. B., Chi, B. X., Lu, H., & Sha, C. N. (2022). Detecting aftershocks of the M_S6.9 Menyuan earthquake and mapping blind faults by a distributed acoustic sensing array with an existing fiber-optic cable. *Chinese Science Bulletin, 67*(27), 3340–3347.

Bigdeli, A., Shishegaran, A., Naghsh, M. A., Karami, B., Shishegaran, A., & Alizadeh, G. (2021). Surrogate models for the prediction of damage in reinforced concrete tunnels under internal water pressure. *Journal of Zhejiang University: Science A, 22*(8), 632–656.

Cao, Y., Zhou, X. K., Yan, K., & Li, D. Y. (2021). Deep learning neural network model for tunnel ground surface settlement prediction based on sensor data. *Mathematical Problems in Engineering, 2021*(1), 9488892.

Chai, W. G., Zheng, Y. X., Tian, L., Qin, J., & Zhou, T. (2023). GA-KELM: Genetic-algorithm-improved kernel extreme learning machine for traffic flow forecasting. *Mathematics, 11*(16).

Chen, G., & Yu, H. T. (2024). Analytical solution for seismic response of composite tunnel liners with arbitrary section shape and embedded with an isolation layer. *Tunnelling and Underground Space Technology, 150*, 105821.

Chen, J. T., Yu, H. T., Bobet, A., & Yuan, Y. (2020). Shaking table tests of transition tunnel connecting TBM and drill-and-blast tunnels. *Tunnelling and Underground Space Technology, 96*, 103197.

Chen, P. L., Geng, P., He, D. W., Wang, T. Q., & He, C. (2024). A novel tool for seismic response analysis of tunnel in multilayered media based on kinematic earthquake source. *Engineering Geology, 340*, 107675.

Chen, P. L., Geng, P., Chen, J. B., & Gu, W. Q. (2023a). The seismic damage mechanism of Daliang tunnel by fault dislocation during the 2022 Menyuan Ms6.9 earthquake based on unidirectional velocity pulse input. *Engineering Failure Analysis, 145*, 107047.

Chen, X., Xiong, Z. M., Zhuge, Y., & Liu, Y. (2023b). Numerical analysis on the seismic performance of subway station in ground crack area. *Tunnelling and Underground Space Technology, 134*, 10501.

Chen, X. S., Shen, J., Bao, X. H., Wu, X. L., Tang, W. C., & Cui, H. Z. (2023c). A review of seismic resilience of shield tunnels. *Tunnelling and Underground Space Technology, 136*, 105075.

Chen, Z. W., & Wang, G. (2023). Comparison of empirically-based and physically-based analyses of coseismic landslides: A case study of the 2016 Kumamoto earthquake. *Soil Dynamics and Earthquake Engineering, 172*, 108009.

China Merchants Chongqing Transportation Research and Design Institute Co., Ltd. (2019). *JTG 2232—2019: Specification for Seismic Design of Highway Tunnel* (in Chinese).

Cornell, C. A., Jalayer, F., Hamburger, R. O., & Foutch, D. A. (2002). Probabilistic basis for 2000 SAC federal emergency management agency steel moment frame guidelines. *Journal of Structural Engineering, 128*(4), 526–533.

Cui, Z., Sheng, Q., Zhang, G. M., Zhang, M. C., & Mei, X. C. (2022a). Response and mechanism of a tunnel subjected to combined fault rupture deformation and subsequent seismic excitation. *Transportation Geotechnics, 34*, 100749.

Cui, Z., Li, J. H., Fu, X. W., Sheng, Q., Zhou, G. X., Ma, Y. L. N., & Wang, T. Q. (2022b). Evaluating the response of a tunnel subjected to strike-slip fault rupture in conjunction with model test and hybrid discrete–continuous numerical modeling. *Rock Mechanics and Rock Engineering, 55*, 4743–4764.

Dai, L., Zhu, Z. D., Zhang, C., & Zhu, D. (2023). Experimental study on the influence of glass fiber reinforced concrete isolation layer on the seismic dynamic response of tunnels. *Case Studies in Construction Materials, 19*, e02303.

Decò, A., Bocchini, P., & Frangopol, D. M. (2013). A probabilistic approach for the prediction of seismic resilience of bridges. *Earthquake Engineering and Structural Dynamics, 42*(10), 1469–1487.

Du, L., Zhang, R., & Fu, Y. G. (2024). A robust evaluating strategy of tunnel deterioration using ensemble machine learning algorithms. *Engineering Applications of Artificial Intelligence, 133*.

Du, X. L., & Zhao, M. (2010). A local time-domain transmitting boundary for simulating cylindrical elastic wave propagation in infinite media. *Soil Dynamics and Earthquake Engineering, 30*(10), 937–946.

Fabozzi, S., Bilotta, E., Picozzi, M., & Zollo, A. (2018). Feasibility study of a loss-driven earthquake early warning and rapid response systems for tunnels of the italian high-speed railway network. *Soil Dynamics and Earthquake Engineering, 112*, 232–242.

Federal Emergency Management Agency (FEMA). (2020). Hazus 4.2 SP3: Hazus earthquake model technical manual.

Firouzi, N., Żur, K. K., Amabili, M., & Rabczuk, T. (2023). On the time-dependent mechanics of membranes via the nonlinear finite element method. *Computer Methods in Applied Mechanics and Engineering, 407*, 115903.

Gu, B., Sheng, V. S., Wang, Z. J., Ho, D., Osman, S., & Li, S. (2015). Incremental learning for ν-support vector regression. *Neural Networks, 67*, 140–150.

Han, K. H., Zhang, D. M., Chen, X. S., Su, D., Ju, J. W. W., Lin, X. T., & Cui, H. Z. (2023). A resilience assessment framework for existing underground structures under adjacent construction disturbance. *Tunnelling and Underground Space Technology*, 141.

Harati, M., & van de Lindt, J. W. (2024). Data-driven machine learning for multi-hazard fragility surfaces in seismic resilience analysis. *Computer-Aided Civil and Infrastructure Engineering, 40*(6), 698–720.

Hasanpour, R., Rostami, J., Schmitt, J., Ozcelik, Y., & Sohrabian, B. (2020). Prediction of TBM jamming risk in squeezing grounds using Bayesian and artificial neural networks. *Journal of Rock Mechanics and Geotechnical Engineering, 12*(1), 21–31.

Hong, H. Y., Liu, J. Z., Bui, D. T., Pradhan, B., Acharya, T. D., Pham, B. T., Zhu, A. X., Chen, W., & Ahmad, B. B. (2018). Landslide susceptibility mapping using J48 decision tree with AdaBoost, Bagging and Rotation Forest ensembles in the Guangchang area (China). *Catena, 163*, 399–413.

Huang, D. W., Zhu, H. H., Shen, Y., Yan, Z. G., & Ju, J. W. W. (2022). Resilient analysis on tunnel structural serviceability based on lifetime dynamic prediction model. *Tunnelling and Underground Space Technology, 129*, 104690.

Huang, H. W., & Zhang, D. M. (2016). Resilience analysis of shield tunnel lining under extreme surcharge: Characterization and field application. *Tunnelling and Underground Space Technology, 51*, 301–312.

Huang, H. W., Zhang, Y. J., Zhang, D. M., & Ayyub, B. M. (2017a). Field data-based probabilistic assessment on degradation of deformational

performance for shield tunnel in soft clay. *Tunnelling and Underground Space Technology, 67*, 107–119.
Huang, J. Q., Du, X. L., Zhao, M., & Zhao, X. (2017b). Impact of incident angles of earthquake shear (S) waves on 3-D non-linear seismic responses of long lined tunnels. *Engineering Geology, 222*, 168–185.
Huang, P. F., Chen, Z. Y., & Liu, Z. Q. (2023). Nonparametric probabilistic seismic demand model and fragility analysis of subway stations using deep learning techniques. *Underground Space, 11*, 63–80.
Huang, S., Xin, C. L., Song, D. Q., Feng, W. K., Liu, X. L., Wang, E. Z., Xu, T. H., & Xiong, X. H. (2024). Resilience assessment of the seismic damage mechanism of the Daliang high-speed railway tunnel in the 2022 Menyuan earthquake (Mw 6.7) in China. *Transportation Geotechnics, 49*, 101417.
Huang, Z. K., Pitilakis, K., Tsinidis, G., Argyroudis, S., & Zhang, D. M. (2020). Seismic vulnerability of circular tunnels in soft soil deposits: The case of Shanghai metropolitan system. *Tunnelling Underground Space Technology, 98*, 103341.
Huang, Z. K., Pitilakis, K., Argyroudis, S., Tsinidis, G., & Zhang, D. M. (2021). Selection of optimal intensity measures for fragility assessment of circular tunnels in soft soil deposits. *Soil Dynamics and Earthquake Engineering, 145*, 106724.
Huang, Z. K., Argyroudis, S. A., Pitilakis, K., Zhang, D. M., & Tsinidis, G. (2022a). Fragility assessment of tunnels in soft soils using artificial neural networks. *Underground Space, 7*(2), 242–253.
Huang, Z. K. (2022b). Resilience evaluation of shallow circular tunnels subjected to earthquakes using fragility functions. *Applied Sciences, 12*(9), 4728.
Huang, Z. K., Zhang, D. M., Pitilakis, K., Tsinidis, G., Huang, H. W., Zhang, D. M., & Argyroudis, S. (2022c). Resilience assessment of tunnels: Framework and application for tunnels in alluvial deposits exposed to seismic hazard. *Soil Dynamics and Earthquake Engineering, 162*, 107456.
Jiang, J. W., El Naggar, M. H., Huang, W. T., Xu, C. S., Zhao, K., & Du, X. L. (2022). Seismic fragility analysis for shallow-buried underground frame structure considering 18 existing subway stations. *Soil Dynamics and Earthquake Engineering, 162*, 107479.
Jiang, J. W., Tao, R., El Naggar, M. H., Liu, H., & Du, X. L. (2024). Seismic performance and fragility analysis for bifurcated tunnels in soft soil. *Computers and Geotechnics, 167*, 106065.
Karami, B., Shishegaran, A., Taghavizade, H., & Rabczuk, T. (2021). Presenting innovative ensemble model for prediction of the load carrying capacity of composite castellated steel beam under fire. *Structures, 33*, 4031–4052.
Kuhlemeyer, R. L., & Lysmer, J. (1973). Finite element method accuracy for wave propagation problems. *Journal of the Soil Mechanics and Foundations Division, 99*(5), 421–427.
Lin, X. T., Chen, X., Su, D., Han, K., & Zhu, M. (2022). An analytical model to evaluate the resilience of shield tunnel linings considering multistage disturbances and recoveries. *Tunnelling and Underground Space Technology, 127*, 104581.
Liu, J. H., Hu, J., Li, Z. W., Ma, Z. F., Shi, J. W., Xu, W. B., & Sun, Q. (2022). Three-dimensional surface displacements of the 8 January 2022 Mw6.7 Menyuan earthquake, China from Sentinel-1 and ALOS-2 SAR observations. *Remote Sensing, 14*(6), 1404.
Long, X. H., Ma, Y. T., Miao, Y., & Ruan, B. (2023). An innovative shape memory alloy flexible circumferential joint for tunnel seismic mitigation. *Tunnelling and Underground Space Technology, 131*, 104783.
Lyu, S., Qi, Q., Huang, X. M., Peng, S. N., Yang, D., & Chen, L. Y. (2024). Machine learning-based method for gas leakage source term estimation in highway tunnels. *Tunnelling and Underground Space Technology, 154*, 106114.
Meng, S. B., Li, W. X., Liu, Z. X., Liu, J. Q., He, W. G., Yang, C. W., Zhao, J. W., & Wei, S. T. (2024). Rapid resilience assessment framework for mountain tunnels subjected to near-fault seismic ground motions. *Soil Dynamics and Earthquake Engineering, 182*, 108746.
Moayedifar, A., Nejati, H. R., Goshtasbi, K., & Khosrotash, M. (2019). Seismic fragility and risk assessment of an unsupported tunnel using incremental dynamic analysis (IDA). *Earthquakes and Structures., 16*(6), 705–714.
Naghsh, M. A., Shishegaran, A., Karami, B., Rabczuk, T., Shishegaran, A., Taghavizadeh, H., & Moradi, M. (2021). An innovative model for predicting the displacement and rotation of column-tree moment connection under fire. *Frontiers of Structural and Civil Engineering, 15*, 194–212.
Qu, L. M., Ding, X. M., Zheng, C. J., Wu, C. R., & Cao, G. W. (2021). Numerical and test study on vertical vibration characteristics of pile group in slope soil topography. *Earthquake Engineering and Engineering Vibration, 20*(2), 377–390.
Rabczuk, T., & Belytschko, T. (2004). Cracking particles: A simplified meshfree method for arbitrary evolving cracks. *International Journal for Numerical Methods in Engineering, 61*(13), 2316–2343.
Rabczuk, T., Zi, G., Bordas, S., & Nguyen-Xuan, H. (2010). A simple and robust three-dimensional cracking-particle method without enrichment. *Computer Methods in Applied Mechanics and Engineering, 199*(37/38/39/40), 2437–2455.
Reddy, A. D., & Singh, A. (2024). A simplistic method for assessing seismic damage in rock tunnels before earthquake: Part 1—damage prediction and validation using seismic damage classification of tunnels. *Rock Mechanics and Rock Engineering, 57*(12), 11001–11032.
Samaniego, E., Anitescu, C., Goswami, S., Nguyen-Thanh, V. M., Guo, H., Hamdia, K., Zhuang, X., & Rabczuk, T. (2020). An energy approach to the solution of partial differential equations in computational mechanics via machine learning: Concepts, implementation and applications. *Computer Methods in Applied Mechanics and Engineering, 362*, 112790.
Shishegaran, A., Boushehri, A. N., & Ismail, A. F. (2020a). Gene expression programming for process parameter optimization during ultrafiltration of surfactant wastewater using hydrophilic polyethersulfone membrane. *Journal of Environmental Management, 264*, 110444.
Shishegaran, A., Khalili, M. R., Karami, B., Rabczuk, T., & Shishegaran, A. (2020b). Computational predictions for estimating the maximum deflection of reinforced concrete panels subjected to the blast load. *International Journal of Impact Engineering, 139*, 103527.
Shishegaran, A., Saeedi, M., Kumar, A., & Ghiasinejad, H. (2020c). Prediction of air quality in Tehran by developing the nonlinear ensemble model. *Journal of Cleaner Production, 259*, 120825.
Shishegaran, A., Moradi, M., Naghsh, M. A., Karami, B., & Shishegaran, A. (2021a). Prediction of the load-carrying capacity of reinforced concrete connections under post-earthquake fire. *Journal of Zhejiang University: Science A, 22*(6), 441–466.
Shishegaran, A., Karami, B., Safari Danalou, E., Varaee, H., & Rabczuk, T. (2021b). Computational predictions for predicting the performance of steel 1 panel shear wall under explosive loads. *Engineering Computations, 38*(9), 3564–3589.
Shishegaran, A., Varaee, H., Rabczuk, T., & Shishegaran, G. (2021c). High correlated variables creator machine: Prediction of the compressive strength of concrete. *Computers & Structures, 247*.
Shishegaran, A., Saeedi, M., Mirvalad, S., & Korayem, A. H. (2023). Computational predictions for estimating the performance of flexural and compressive strength of epoxy resin-based artificial stones. *Engineering with Computers, 39*(1), 347–372.
Sun, W. Y., Lin, J. C., Ma, Q. G., Yan, S. H., Tong, H., & Liang, Q. G. (2024). Seismic fragility assessment of circular metro tunnels in loess deposit. *Journal of Central South University, 31*(3), 950–964.
Sun, Y., Feng, X. D., Yang, L. Q., & Chastre, C. (2018). Predicting tunnel squeezing using multiclass support vector machines. *Advances in Civil Engineering, 2018*(1).
Tian, H. X., & Mao, Z. Z. (2010). An ensemble ELM based on modified AdaBoost.RT algorithm for predicting the temperature of molten steel in ladle furnace. *IEEE Transactions on Automation Science and Engineering, 7*(1), 73–80.
Tian, J. W., Liu, Y., Zheng, W. F., & Yin, L. R. (2022). Smog prediction based on the deep belief - BP neural network model (DBN-BP). *Urban Climate, 41*, 101078.
Tsinidis, G., Karatzetzou, A., Stefanidou, S., & Markogiannaki, O. (2022). Developments in seismic vulnerability assessment of tunnels and underground structures. *Geotechnics, 2*(1), 209–249.
Tsinidis, G., Stefanidou, S., & Karatzetzou, A. (2024a). New limit states for the seismic fragility assessment of circular tunnels: Application in case of tunnels in clayey soil deposits. *Tunnelling and Underground Space Technology, 154*, 106129.
Tsinidis, G., Karatzetzou, A., & Stefanidou, S. (2024b). On the effects of salient parameters for an efficient assessment of seismic response and fragility of circular tunnels in clayey deposits. *Soil Dynamics and Earthquake Engineering, 178*, 108490.

Wang, L. J., Geng, P., Chen, J. B., & Wang, T. Q. (2023a). Machine learning-based fragility analysis of tunnel structure under different impulsive seismic actions. *Tunnelling and Underground Space Technology, 133*, 104953.

Wang, Q., Geng, P., Li, P. S., He, D. W., & Shen, H. M. (2024). Failure analysis of circumferential joints and preferable bolt form of shield tunnel under normal fault dislocation. *Tunnelling and Underground Space Technology, 146*, 105648.

Wang, Y., Wang, Q., Zhong, X. M., & Deng, J. (2023b). Seismic response analysis of the Daliang tunnel during the Menyuan M_S6.9earthquake. *China Earthquake Engineering Journal, 45*(6), 1315–1323, 1332 (in Chinese).

Wen, Y. M., Xin, C. L., Shen, Y. S., Huang, Z. M., & Gao, B. (2021). The seismic response mechanisms of segmental lining structures applied in fault-crossing mountain tunnel: The numerical investigation and experimental validation. *Soil Dynamics and Earthquake Engineering, 151*, 107001.

Wu, Y. L., Ke, Y. T., Chen, Z., Liang, S. Y., Zhao, H. L., & Hong, H. Y. (2020). Application of alternating decision tree with AdaBoost and bagging ensembles for landslide susceptibility mapping. *Catena, 187*.

Xin, C. L., Wang, Z. Z., Zhou, J. M., & Gao, B. (2019). Shaking table tests on seismic behavior of polypropylene fiber reinforced concrete tunnel lining. *Tunnelling and Underground Space Technology, 88*, 1–15.

Xin, C. L., Wang, Z. Z., & Gao, B. (2018). Shaking table tests on seismic response and damage mode of tunnel linings in diverse tunnel-void interaction states. *Tunnelling and Underground Space Technology, 77*, 295–304.

Xin, C. L., Wang, Z. Z., & Yu, J. (2020). The evaluation on shock absorption performance of buffer layer around the cross section of tunnel lining. *Soil Dynamics and Earthquake Engineering, 131*, 106032.

Xin, C. L., Wang, Z., Hajirasouliha, I., Yang, F., Li, W. H., Chen, T., & Gao, B. (2022). Seismic response mechanisms of casing-shape composite tunnel lining: Theoretical analysis and shaking table test verification. *Soil Dynamics and Earthquake Engineering, 162*, 107440.

Xin, C. L., Shuai, Y. X., Song, D. Q., & Liu, X. L. (2024a). Dynamic interaction and failure mechanism in tunnel-slope systems: Mitigation insights from shaking table tests and numerical analysis. *Tunnelling and Underground Space Technology, 152*, 105940.

Xin, C. L., Feng, W. K., Song, D. Q., Huang, S., & Liu, X. L. (2024b). Seismic damage to non-fault-crossing and fault-crossing tunnels: Comparative study of the 2008 Wenchuan earthquake (Mw 7.9) and the 2022 Menyuan earthquake (Mw 6.7). *Engineering Failure Analysis, 166*, 108843.

Xing, H. J., Liu, W. T., & Wang, X. Z. (2024). Bounded exponential loss function based AdaBoost ensemble of OCSVMs. *Pattern Recognition, 148*, 110191.

Yu, H. T., Chen, J. T., Bobet, A., & Yuan, Y. (2016). Damage observation and assessment of the Longxi tunnel during the Wenchuan earthquake. *Tunnelling and Underground Space Technology, 54*, 102–116.

Zhang, C. L., Zhang, B., Zhang, D. M., Huang, Z. K., & Huang, H. W. (2025). Machine learning-based resilience assessment of tunnel under explosions: Integrating post-explosion loss and recovery models. *Computers and Geotechnics, 179*, 107008.

Zhang, Y. F., Yuan, K., Zhou, W. J., & Fan, J. W. (2023a). Study on structural deformation characteristics and surface crack distribution of Daliang tunnel across Lenglongling fault caused by Menyuan earthquake. *Chinese Journal of Rock Mechanics and Engineering, 42*(5), 1055–1069 (in Chinese).

Zhang, Y. F., Chen, J., Gong, W. Y., Han, N. N., Liu, Y. H., & Shan, X. J. (2023b). Geodetic modelling of the 2022 Mw6.6 Menyuan earthquake: Insight into the strain-partitioned northern Qilian Shan fault system and implications for regional tectonics and seismic hazards. *Geophysical Journal International, 233*(3), 1987–2003.

Zhong, Z. L., Wang, Z., Zhao, M., & Du, X. L. (2020). Structural damage assessment of mountain tunnels in fault fracture zone subjected to multiple strike-slip fault movement. *Tunnelling and Underground Space Technology, 104*, 103527.

Zhou, H., He, C. D., Wang, X., Chen, Y. J., & Li, J. (2021). Assessment of the Seismic Response of Shallow buried Elliptical Tunnels. *Journal of Earthquake Engineering, 27*(3), 465–487.

Zhu, H. H., Yu, H. T., Han, F. Q., Wei, Y. B., & Yuan, Y. (2023). Seismic Resilience Design Principles and Key Issues for Tunnels Crossing active Faults. *China Journal of Highway and Transport, 36*(11), 193–204 (in Chinese).